PB92-206853

Remote Sensing Data from CLARET: A Prototype Cart Data Set

(U.S.) National Oceanic and Atmospheric Administration, Boulder, CO

Jun 92

BIBLIOGRAPHIC INFORMATION

PB92-206853

Report Nos: NOAA-TM-ERL-WPL-223

Title: Remote Sensing Data from CLARET: A Prototype Cart Data Set.

Date: Jun 92

Authors: W. L. Eberhard, T. Uttal, K. A. Clark, R. E. Cupp, and E. G. Dutton.

Performing Organization: National Oceanic and Atmospheric Administration, Boulder, CO. Wave Propagation Lab.

Type of Report and Period Covered: Technical memo.

Supplementary Notes: See also DE90008108.

NTIS Field/Group Codes: 55E, 55C

Price: PC A04/MF A01

Availability: Available from the National Technical Information Service, Springfield, VA. 22161

Number of Pages: 65p

Keywords: *Clouds(Meteorology), *Remote sensing, *Meteorologic data, *Atmospheric radiation, US DOE, Meteorological instruments, Cloud cover, Cloud height indicators, Cirrus clouds, Stratus clouds, Terrestrial radiation, *Cloud Lidar and Radar Exploratory Test, Atmospheric Radiation Measurement, Cloud and Radiation Testbed.

Abstract: The data set containing radiation, meteorological, and cloud sensor observations is documented. It was prepared for use by the Department of Energy's Atmospheric Radiation Measurement (ARM) program and other interested scientists. These data are a precursor of the types of data that ARM Cloud And Radiation Testbed (CART) sites will provide. The data are from the Cloud Lidar And Radar Exploratory Test (CLARET) conducted by the Wave Propagation Laboratory during autumn 1989 in the Denver-Boulder area of Colorado primarily for the purpose of developing new cloud-sensing techniques on cirrus. After becoming aware of the experiment, ARM scientists requested archival of subsets of the data to assist in the developing ARM program. Five CLARET cases were selected: two with cirrus, one with stratus, one with mixed-phase clouds, and one with clear skies. Satellite data from the stratus case and one cirrus case were analyzed for statistics on cloud cover and top height. The main body of the selected data are available on diskette from the Wave Propagation Laboratory or Los Alamos National Laboratory.

NOAA Technical Memorandum ERL WPL-223

REMOTE SENSING DATA FROM CLARET: A PROTOTYPE CART DATA SET

Wynn L. Eberhard
Taneil Uttal
Kurt A. Clark
Richard E. Cupp
Ellsworth G. Dutton
Leonard S. Fedor
Janet M. Intrieri
Sergey Y. Matrosov
Jack B. Snider
Ron J. Willis

Wave Propagation Laboratory
Boulder, Colorado
June 1992

noaa NATIONAL OCEANIC AND ATMOSPHERIC ADMINISTRATION / Environmental Research Laboratories

NOAA Technical Memorandum ERL WPL-223

REMOTE SENSING DATA FROM CLARET: A PROTOTYPE CART DATA SET

Wynn L. Eberhard
Taneil Uttal
Kurt A. Clark
Richard E. Cupp
Ellsworth G. Dutton
Leonard S. Fedor
Janet M. Intrieri
Sergey Y. Matrosov
Jack B. Snider
Ron J. Willis

Wave Propagation Laboratory
Boulder, Colorado
June 1992

UNITED STATES DEPARTMENT OF COMMERCE

Barbara Hackman Franklin
Secretary

NATIONAL OCEANIC AND ATMOSPHERIC ADMINISTRATION

John A. Knauss
Under Secretary for Oceans and Atmosphere/Administrator

Environmental Research Laboratories

Joseph O. Fletcher
Director

NOTICE

Mention of a commercial company or product does not constitute an endorsement by the NOAA Environmental Research Laboratories. Use of information from this publication concerning proprietary products or the tests of such products for publicity or advertising purposes is not authorized.

For sale by the National Technical Information Service, 5285 Port Royal Road
Springfield, VA 22061

TABLE OF CONTENTS

Page

REMOTE SENSING DATA FROM CLARET: A PROTOTYPE CART DATA SET

Wynn L. Eberhard[1], Taneil Uttal[1], Kurt A. Clark[1],
Richard E. Cupp[1], Ellsworth G. Dutton[2], Leonard S. Fedor[1],
Janet M. Intrieri[3], Sergey Y. Matrosov[3], Jack B. Snider[1],
and Ron J. Willis[3]

ABSTRACT

A data set containing radiation, meteorological, and cloud sensor observations is documented. It was prepared for use by the Department of Energy's Atmospheric Radiation Measurement (ARM) program and other interested scientists. These data are a precursor of the types of data that ARM Cloud And Radiation Testbed (CART) sites will provide. The data are from the Cloud Lidar And Radar Exploratory Test (CLARET) conducted by the Wave Propagation Laboratory during autumn 1989 in the Denver-Boulder area of Colorado primarily for the purpose of developing new cloud-sensing techniques on cirrus. After becoming aware of this experiment, ARM scientists requested archival of subsets of the data to assist in the developing ARM program.

Five CLARET cases were selected: two with cirrus, one with stratus, one with mixed-phase clouds, and one with clear skies. The cases range from 2 to 9.5 h in length. A pyranometer, pyrgeometer, pyrheliometer, and an infrared radiometer constituted the ensemble of instruments that provided surface radiation data. A lidar, radar, and ceilometer observed the cloud geometrical structure, and visual reports and all-sky camera observations were assimilated to provide cloud cover data. Radiosondes, wind profiler, RASS (profiling virtual temperature), microwave radiometers (observing column-integrated liquid water and water vapor), and standard surface measurements provided meteorological data. Satellite data from the stratus case and one cirrus case were analyzed for statistics on cloud cover and top height. The main body of the selected data are available on diskette from the Wave Propagation Laboratory or Los Alamos National Laboratory.

---

[1]Wave Propagation Laboratory, NOAA/ERL, Boulder, CO

[2]Climate Monitoring and Diagnostics Laboratory, NOAA/ERL, Boulder, CO

[3]Cooperative Institute for Research in Environmental Sciences, Boulder, CO

In addition to documenting the data set, this report describes CLARET and gives a bibliography of publications associated with the project. Some preliminary results of CLARET research are also summarized. Simultaneous CO_2 lidar and radar backscatter measurements were shown to provide estimates of the effective radius of ice particles. Simultaneous radar and infrared radiometer data appear useful for estimating column-integrated numbers and average sizes of ice cloud particles. Ice water content obtained with this method compared favorably with values from another empirical technique using radar data alone. Depolarization of the CO_2 lidar signal from ice clouds was surprisingly small, suggesting that calculation of backscatter from nonspherical particles for this lidar is a tractable problem. Examples are also cited of CO_2 lidar measurements of the effective radius of water cloud drop size distributions and of inference of the size of pristine ice crystals that assume a particular orientation in the air. These parameters are all important to radiative transfer through clouds.

1. INTRODUCTION

The Department of Energy (DOE) has embarked on a major research effort called the Atmospheric Radiation Measurement (ARM) Program (DOE, 1990). The experimental portion of ARM will center around Cloud And Radiation Testbed (CART) sites. The Wave Propagation Laboratory (WPL) conducted the Cloud Lidar And Radar Exploratory Test (CLARET) with a combination of instruments in a research mode that bears a strong resemblance to the configuration planned for CART sites. This report documents condensed data sets from five events during CLARET that have been prepared for use by ARM and other scientists as a precursor of the type of data anticipated from CART.

1.1 Background and Goals of ARM

Most experts agree that increases in atmospheric CO_2 from burning of fossil fuels will cause a warming of the global climate. The atmosphere is a very complex physical system, and global circulation models (GCMs) seem to be the only method for accurately predicting climate change, especially on the regional scale. Deficiencies in current GCMs prevent them from predicting climate change with accuracy sufficient for answering issues of public policy regarding climate change. The effects of clouds, and, in particular, the feedback role of clouds during climate change, constitute a large source of uncertainty in climate GCMs (Cess et al., 1990).

DOE plans (DOE, 1990) to overcome these limitations by advancing computer technology to accommodate better models, by training a new generation of climate scientists, and by conducting ARM to improve GCM parameterizations of clouds and radiation. ARM has three goals: First is to develop an accurate quantitative description of the spectral

radiative energy balance profile under a wide variety of meteorological conditions. Second is to understand the processes controlling the radiative balance, including comprehensive field observations of cloud effects and comparison of the observations with models. Third is to use this knowledge to improve parameterizations in GCMs, with a major emphasis on the role of clouds.

The experimental phase will be accomplished at several well-instrumented CART sites at key locations on the globe. Each facility will measure radiation and meteorological parameters to the fullest practical extent as a function of height and time within a three-dimensional volume of horizontal extent corresponding to a GCM grid cell. Data from the CART facilities will be used to develop and verify radiative transfer codes.

1.2 Background of CLARET

WPL conducts research and development involving several surface-based instruments that observe various properties of clouds and also of the clear atmosphere. These include lidar, radar, microwave radiometer, and meteorological profiler systems. Other divisions of the Environmental Research Laboratories in Boulder, Colorado, have additional sensing capabilities; noteworthy among these are measurements of surface radiation by CMDL (Climate Monitoring and Diagnostics Laboratory).

During autumn 1989, WPL conducted the experimental phase of CLARET. Coordinated measurements were obtained of radiation, clouds, and meteorological parameters by many sensors, some continuously, and others on an episodic basis. The main objective of CLARET was to improve and develop new remote sensing techniques for observing parameters of clouds, especially cirrus, that are important to climate. Our measurements are also WPL's contribution to the international Experimental Cloud Lidar Pilot Study (ECLIPS; WMO, 1988; Platt, 1991). Although this report for ARM was not part of the original CLARET plan, the Los Alamos National Laboratory (LANL) of DOE soon recognized the excellent potential for deriving a precursor CART data set from CLARET observations.

1.3 Objectives of the Current Project

Our objective in this project for DOE is to make available data sets from several CLARET cases to assist in the early development of the ARM program. These data provide examples to guide the design of CART instrumentation and data acquisition systems. Modelers can also use the data as a precursor of the products a CART site will supply. In addition, some of the cases were selected to match the research interests of Los Alamos scientists in particular kinds of cloud events.

Included in this report are the following:

(1) a description of the CLARET experiment and instrumentation,

(2) documentation of the data sets prepared for DOE,

(3) preliminary research results from the CLARET program, including cloud information that can be derived from instruments used in combination,

(4) bibliography of publications describing CLARET and results, and

(5) recommendations for ARM and CART development based on WPL's experience during CLARET and other projects.

2. CLARET

2.1 Objectives

The measurement of various cloud parameters has always been a challenging part of atmospheric science. The concern about cloud effects on climate has increased the need for cloud observations, including some parameters for which data are sparse or nonexistent. Little is known about ice clouds, especially cirrus, compared with other major cloud types. They are difficult to access, satellite measurements are often deficient because cirrus optical depths are frequently small, and the bulk and microphysical characteristics of ice clouds are highly variable. Although data were acquired on a variety of cloud types, CLARET principally examined middle and high ice clouds.

One example of a poorly observed parameter is effective radius of cirrus particles. Stephens et al. (1990) showed by modeling that the magnitude and even the sign of cirrus cloud feedback during climate change depend on the size distribution (i.e., effective radius) of the cloud particles. Traditionally, experimenters have measured size distribution with instrumented aircraft. The procedure is difficult, because of the high altitude of the clouds and the complexity of data reduction, so results are not very extensive. The summary by Dowling and Radke (1990) shows that the size distributions are highly variable. Therefore, a strong need exists for a simple method to measure effective radius of cirrus particles. Better and simpler methods to obtain many other parameters are also important to the success of cloud and radiation research.

Radar and lidar offer considerable potential for filling some of these needs. Part of the potential arises out of technological improvements, such as increased sensitivity of radar. The advent of CO_2 lidar, which operates at 10.6 μm or other nearby wavelengths, also brings new opportunities. The interaction of radiation at the CO_2 lidar's wavelength with cloud

particles differs considerably from the interaction of the traditional shortwave lidars at visible or near-visible wavelengths. CLARET sought innovative use of signals from individual or combined instruments to supply new parameters and better insights about clouds.

The objectives of CLARET are to

(1) evaluate the potential of CO_2 lidar for remote sensing of clouds, including development of new techniques to measure parameters that are uniquely addressable at its wavelength,

(2) develop new techniques to measure cloud parameters through combined measurements by two or more different instruments (e.g., radar and lidar), and

(3) perform case studies with simultaneous data from several instruments to learn more about cloud properties.

2.2 Description of Experiment

WPL performed the CLARET measurements during the period September 6 through October 5, 1989. The primary instruments were positioned in a cluster (Fig. 1) at the Boulder Atmospheric Observatory (BAO) so that they could simultaneously observe the same region of cloud. Instruments at Stapleton Airport (SA) and at WPL's wind profiler and RASS site near Platteville supplied additional measurements. Data were also collected from NOAA's Geostationary Operational Environmental Satellite (GOES) and Advanced Very High Resolution Radiometer (AVHRR) satellites, encompassing an area larger than the state of Colorado. Table 1 lists the sensors and the fundamental parameters they observed. Details about these instruments and the information derived from them during CLARET are given in Section 2.4.

The BAO, SA, and Platteville sites are on the plain just east of the Rocky Mountains. The "peaks" in Fig. 1 indicate the location of the eastern foothills of these mountains; the Continental Divide is about 60 km west of the BAO. These mountains were sometimes a major factor in the formation of the clouds measured over the BAO.

The measurements during the month-long field phase of CLARET were performed in two different modes, intensive and monitoring. We attempted to operate all instruments during intensive episodes. Those instruments labeled "E" in Table 1 usually provided data only during intensive periods. The lidars are included in this category, because each required an operator. The conditions that triggered an intensive period were the forecast or presence of desired cloud conditions, the availability of required personnel, and the timing of an AVHRR overpass with adequate nadir angle toward the BAO. Most of the intensive episodes were during daylight, but some continued past sunset.

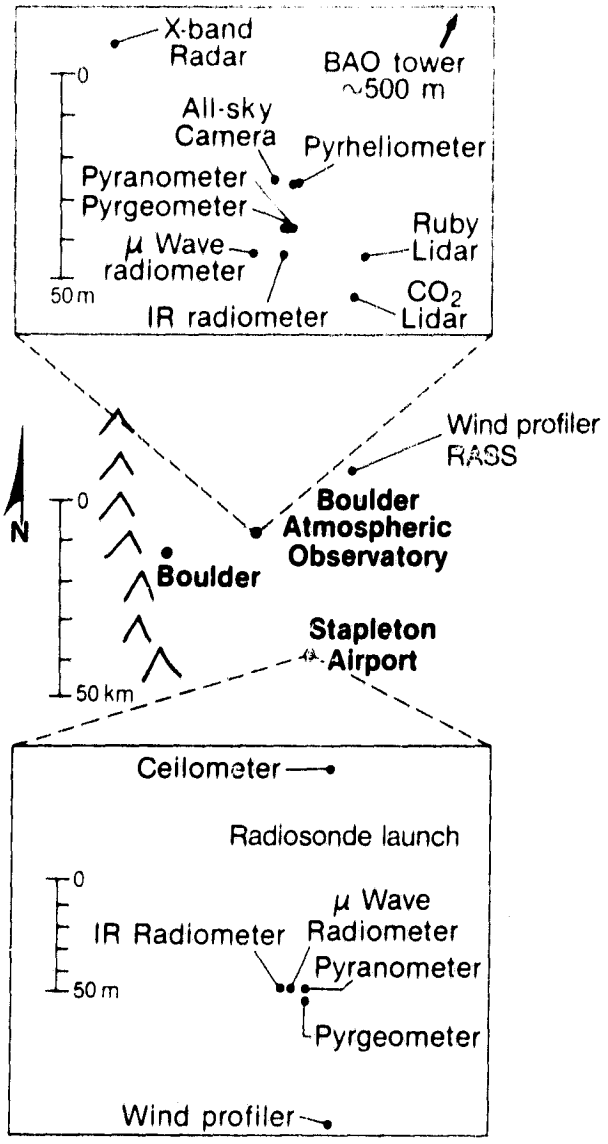

Fig. 1. Locations of surface-based CLARET sensors. Magnified views are shown of the BAO and SA sites. The Platteville wind profiler and RASS instruments are northeast of the BAO.

The instruments labeled by a "C" in Table 1 operated continuously, and all their data were archived for later access. The "I" in Table 1 designates instruments that supplied data to CLARET at regular intervals, e.g., the twice daily radiosonde soundings by the National Weather Service (NWS) at SA.

The radar was the only instrument that switched between intensive and automated monitoring modes. It required an operator during intensive episodes to operate at maximum data rates and to occasionally survey the sky with scans. During monitoring periods, the unattended radar acquired data at a much slower rate while pointed at the zenith.

The intensive periods were typically 1-3 h in duration centered on AVHRR overpass times. Intensive operations sometimes continued between AVHRR overpasses when cloud conditions were excellent. Data from all primary instruments are available for 10 cases, where a case is one of these 1-3 h periods. During six of these cases, we observed principally ice clouds overhead. During one case, the observed clouds contained only water, and during three cases, the sky was clear of clouds overhead. An additional 12 cases were just as successful, except data from one primary instrument were missing, usually from the AVHRR or the CO_2 lidar. Several more cases lacked data from two or more of the "E" instruments, and many cases are available from the monitoring mode. CLARET provided many cases that could adequately serve as precursors of CART data.

A bibliography of publications describing CLARET and some results is in Appendix A.

Table 1. CLARET instruments, operating schedule, and wavelengths or frequencies

Instrument	When*	Wavelength or Frequency
Ruby lidar	E	0.694 μm
CO_2 lidar	E	10.59 μm
Radar	E,C	3.2 cm
Microwave radiometer (BAO)	C	20.6, 31.65, 90.0 GHz
Microwave radiometer (SA)	C	20.6, 31.65, 52.85, 53.85, 55.45, 58.80 GHz
Pyranometers	C	0.28-2.8, 0.695-2.8 μm
Pyrgeometers	C	4-50 μm
IR radiometer (BAO)	E	9.95-11.43 μm
IR radiometer (SA)	C	9.95-11.43 μm
Pyrheliometer	C	0.28-2.8, 0.695-2.8 μm
AVHRR (NOAA 10,11)	E	0.6, 0.9, 3.7, 10.8, 12.0 μm
GOES	I	Visible, 6.7, 7.3, 11.2, 12.7 μm
Wind profilers	C	50, 915 MHz
RASS	C	50 MHz and acoustic
All-sky camera and zenith video	E	Visible
Ceilometer	C	0.904 μm
Surface meteorology	C	---
Radiosonde	I	---

*C, continuous; E, episodic; I, intervals

2.3 Selected Cases

The cases selected are summarized in Table 2. Each of these events included an intensive operating period, but some cases also extended into a period of monitoring mode. A synopsis of the conditions and data available for each case is given in Section 3.

Table 2. Cases selected for CART precursor data sets

Day #	Date	Time (UTC)	Cloud Type
271	September 28	1400-1630	Cirrus
273	September 30	1450-1700	Clear
276	October 3	1200-2130	Stratus
277	October 4	1900-2120	Mixed Phase
278	October 5	1415-1615	Cirrus

2.4 Instruments and Parameters Measured

This subsection describes the individual CLARET instruments, the parameters they measured, and the data products included in the example data sets. Section 4 gives some preliminary results from our research on new cloud-sensing techniques that go beyond the more fundamental data products described in this section.

2.4.1 Shortwave (Ruby) Lidar

WPL's ruby lidar (Eberhard and McNice, 1986) was one of two research lidars in CLARET. The ruby lidar transmitted at 0.6943-μm wavelength with typically 0.5-J pulse energy, approximately 40-ns pulse length, and 1-mr divergence angle. The fastest pulse repetition rate of 1/3 Hz was used during intensive periods when the clouds overhead were rapidly varying. The pulse rate ranged to as slow as 1/30 Hz during some monitoring periods when we happened to have staff at the site. The receiver's field of view was 6 mr. The operator altered the system's sensitivity to optimally match the dynamic range of the 8-bit digitizers by changing the optical density of filters in the receiver and also by adjusting the high voltage bias applied to the photomultiplier detectors. The backscatter signal from each pulse was digitized at 7.5-m range intervals and later averaged to 15-m range gates.

The lidar was aimed at the zenith most of the time. On a few occasions, the elevation angle was scanned back and forth a few degrees about the vertical for the purpose of studying the enhanced backscatter from hexagonal plate crystals with their flat sides oriented horizontally. Sometimes the lidar was aimed a degree or two off zenith to decrease the effects of enhanced backscatter.

The receiver had two channels for simultaneous detection of vertical and horizontal linear polarizations. The transmitted light was linearly polarized in the horizontal.

One standard product of our processing after the experiment was the range-resolved apparent backscatter coefficient. This parameter is the sum of the horizontal and vertical backscatter, each corrected for range and lidar sensitivity, but not corrected for attenuation by the atmosphere or the clouds. A second standard product was the linear depolarization ratio δ_1, which is the vertical/horizontal ratio of backscatter, i.e., the orthogonal/parallel ratio of polarizations relative to the transmitted polarization. Both of these parameters were displayed in color-encoded time-height diagrams with no pulse averaging.

The example data sets in this report give the cloud base height (m AGL) and penetration depth (m) at 30-s intervals derived from the ruby lidar profiles of apparent backscatter coefficient. The cloud base height was determined by averaging the profiles within the 30-s period and finding the lowest range gate in which the backscatter exceeded an appropriate threshold. This threshold was set large enough to avoid false reports by noise or by strong signal from the aerosol in the lower troposphere, yet small enough to pick up the lower edge of the cloud as interpreted from the time-height diagrams. The threshold was subjectively adjusted by a few decibels to allow for varying cloud, aerosol, and noise conditions.

The penetration depth was determined in a similar way by finding the highest range gate in which the backscatter exceeded a threshold. This threshold was often the same as that for cloud base, but sometimes was smaller. The penetration depth can be interpreted in two different ways, depending on the optical depth of the cloud. When the cloud is optically thick (as is usually the case for stratus clouds), the penetration depth gives the height above cloud base where the signal diminishes to an undetectable level because of attenuation. When the cloud is not so thick (as is usually the case for cirrus clouds), the penetration depth gives the distance between cloud base and cloud top. As an illustration, cloud boundaries derived from the ruby lidar data for the October 4 case are plotted in Fig. 2.

The depolarization ratio at this lidar's wavelength discriminates between ice ($\delta_1 \sim 0.5$) and water ($\delta_1 \sim 0$) clouds, as discussed by Sassen (1991). One complication is that multiple scatter in dense water clouds can introduce substantial depolarization. Another complication for a zenith-pointing lidar is that ice plates oriented with their faces horizontal will produce enhanced backscatter with small δ_1. We did not include any tables of δ_1 values in the archived data set because of these complexities in interpretation and the large volume of data.

However, false-color displays of the apparent backscatter and depolarization measurements can be made available for collaborative research. The descriptions of our example data cases in this report do include information on the ruby lidar's depolarization signatures.

The ruby lidar provided data for all of the example data sets highlighted in this report.

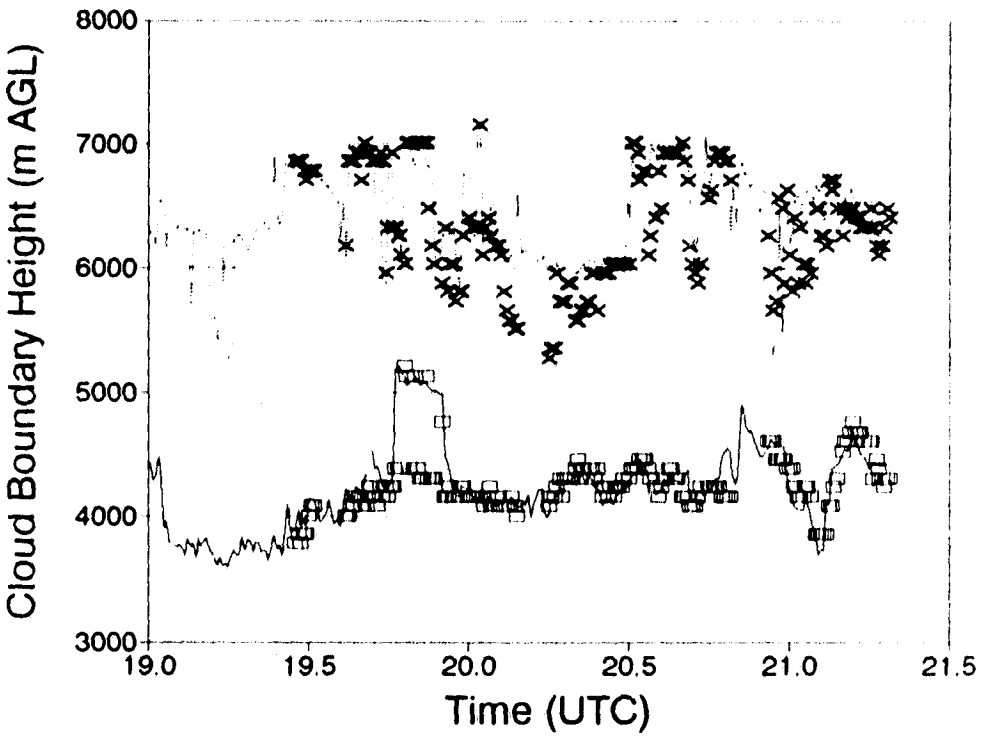

Fig. 2. Cloud base heights and "top" heights (upper limits of detectable signal) from lidar data on October 4. Lines are from the ruby lidar, and squares and crosses are from the CO_2 lidar.

2.4.2 Infrared CO_2 Lidar

The second research lidar in CLARET was a CO_2 lidar transmitting at 10.59 μm wavelength. Systems operating at this wavelength are relatively new in the lidar community and have not yet been used extensively in cloud sensing. The backscatter of a CO_2 lidar from clouds will have different characteristics than those of the more familiar shortwave lidars. One reason is that the scattering size parameter is more than an order of magnitude smaller at

the IR wavelength than for shortwave lidars. Perhaps even more important, water and ice are both highly absorbing at CO_2 lidar wavelengths, whereas scattering dominates for shortwave lidars. One of our main objectives in CLARET was to evaluate the information CO_2 lidar can provide on clouds and investigate techniques that may be unique to IR lidar wavelengths.

Post and Cupp (1990) described the lidar, which we operated in a short-pulse mode (Eberhard et al., 1989) with 0.4-μs pulse length. The divergence angle and field of view of this diffraction-limited system was about 0.1 mr. The pulse repetition rate was usually 8 Hz, and the polarization state alternated every 10 pulses (details are given in Section 4.4). Pulses were averaged later to obtain the backscatter and depolarization each 2.5 s. Electronic filtering in the amplifier chain after the detector was sometimes required to avoid saturating the 8-bit signal digitizer. The lidar performs coherent detection, so the detector output is proportional to the amplitude of the electric vector of the light. The dynamic range was therefore equivalent to that of a 16-bit detector in a power-detecting shortwave lidar. The digitizer sampled at 15-m range intervals, and data were later averaged to 75-m range gates.

Like the ruby lidar, the CO_2 lidar usually pointed at the zenith, but sometimes rocked in elevation angle a few degrees off zenith.

The CO_2 lidar is a Doppler system that can measure the radial (along-beam) velocity component of the scatterers. The accuracy of this current system is typically about 0.5 m s^{-1}, which is substantial compared with vertical motions of cloud particles. CLARET concentrated on studying information from the backscatter, and we have not attempted to extract vertical velocities from the data.

The apparent backscatter coefficient and depolarization profiles were calculated and displayed in a manner similar to that for the ruby lidar, and can be made available to collaborators. The CO_2 lidar's apparent backscatter coefficients include a correction for molecular absorption by the atmosphere.

The CO_2 lidar consistently measured small depolarizations from clouds. The reasons are discussed in Section 4.4. Cloud base heights (m AGL) and penetration depths (m) were obtained using the same technique as for the ruby lidar. An example of results from October 4 is shown in Fig. 2. These height parameters are included in the examples presented for the cases when the CO_2 lidar operated.

2.4.3 Radar

WPL's 3.2-cm-wavelength scanning radar is capable of measurements of velocity (± 0.1 m s^{-1}), Doppler spectral width, reflectivity factor, and circular depolarization. A major advantage of this radar for climate studies is that it can be operated unattended for 24-48 h periods. During CLARET, the radar operated with 125-m pulse length, 75-m range gate spacing, and maximum range of 24 km. The dwell time of 0.4 s was longer than

commonly used for observing cumulus or precipitating stratus clouds. The radar collected data in two modes, monitoring and intensive. In the monitoring mode, the radar recorded data for 0.4 s then paused for 3.4 s. In the intensive mode, the radar recorded data with 0.4 s sampling periods without gaps between. For this report, the intensive data were processed later to make an effective dwell time of 4 s, and then 30-s averages were formed from data in either mode to match the averaging periods of the microwave and IR radiometers.

The data set prepared for this report includes the time series of cloud base height and cloud thickness or top height. These were determined by a threshold test on the 4-s data, and averaging the heights successfully found for a 30-s period. Figure 3 gives an example from the October 4 case. The column-integrated ice content (or ice water path) was also calculated from an empirical algorithm relating reflectivity to ice water content as determined by Sassen (1987); an example is shown in Fig. 4. False-color displays of the more detailed reflectivity and velocity data can be supplied if needed.

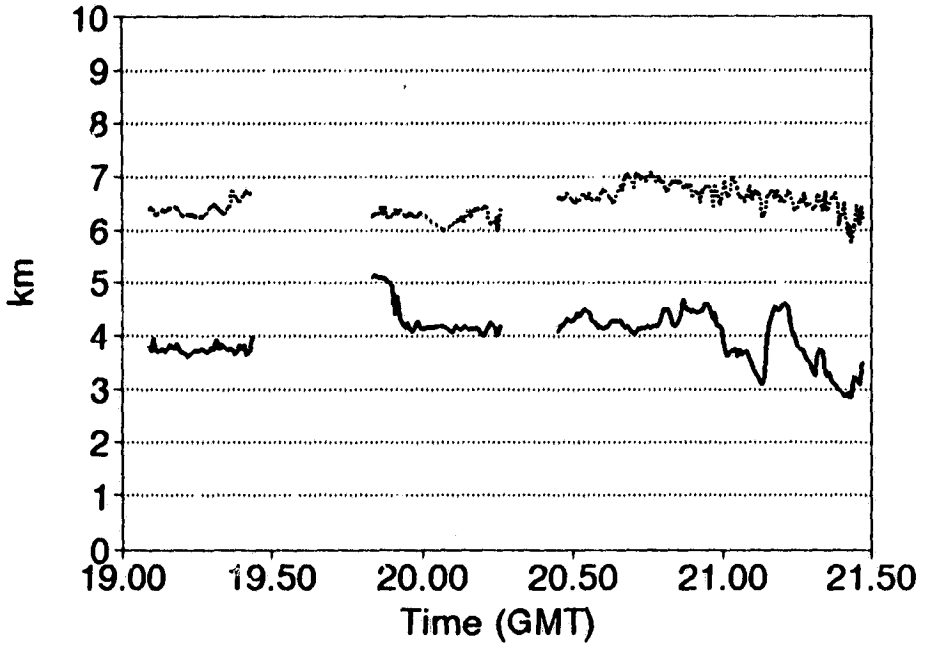

Fig. 3. Cloud boundary heights (km AGL) based on radar signal for the October 4 case.

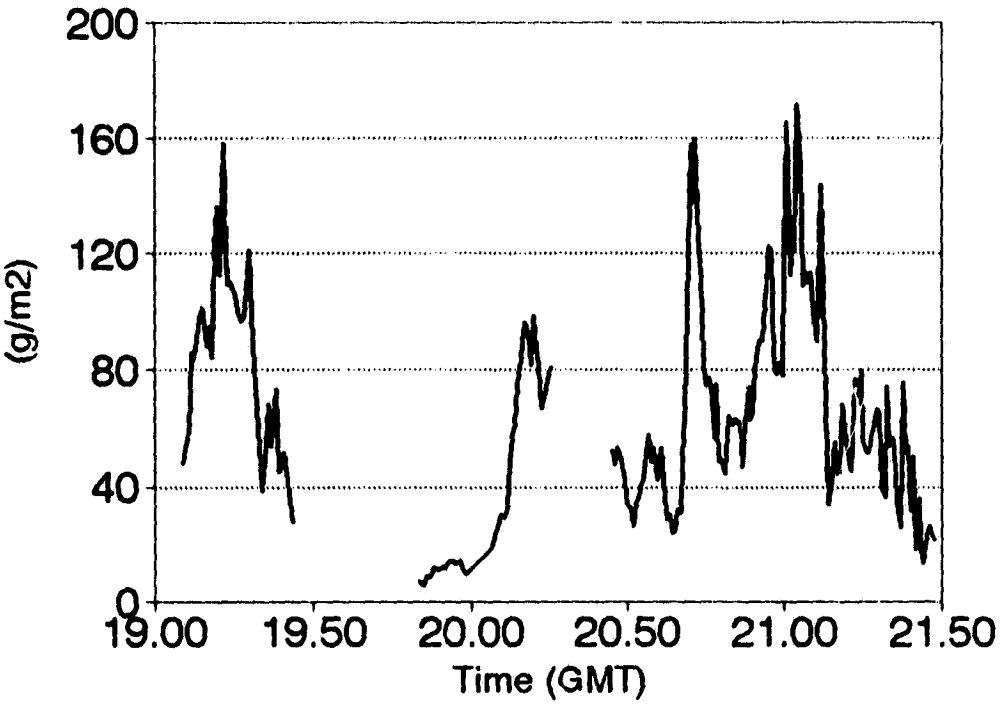

Fig. 4. Column-integrated ice water content, or IWP, on October 4 calculated from the radar reflectivity using the algorithm of Sassen (1987).

2.4.4 Microwave Radiometer

The WPL microwave radiometer is a passive system that simultaneously measures liquid water in clouds and precipitable water vapor in the atmosphere (Hogg et al., 1983). The system operated at the BAO contains three independent radiometers sharing a common antenna. The first operates at 20.6 GHz, which is sensitive primarily to water vapor. The second operates at 31.7 GHz, which is sensitive primarily to liquid water at any temperature. The third operates at 90.0 GHz, which is sensitive to both liquid and vapor, but is 6 times more sensitive than the 31.7-GHz channel to liquid water. This third channel is experimental, and was not included in deriving results for CLARET. The SA microwave radiometer did not have the 90.0 GHz channel, but has four additional channels for sensing temperature profiles. The vertical resolution of these are quite coarse and are excluded from the data archived in this study. Because of the low emission of microwaves by ice, the radiometer is insensitive to ice. The processed data are 30-s averages of the total path-integrated water vapor (cm) and liquid water (mm) from the first two channels. Example data from October 4 are given in Fig. 5.

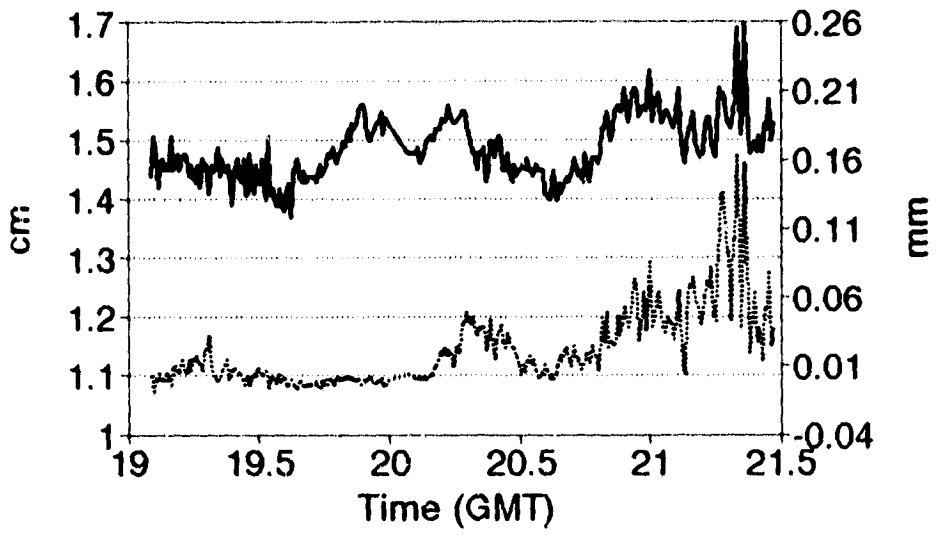

Fig. 5. Column-integrated water vapor in cm (solid line) and liquid water in mm (dotted line), both measured by the microwave radiometer at the BAO during the October 4 case.

The sensitivity of the microwave radiometer to liquid water is typically 0.01 mm but may be as large as about 0.02 mm. When measurements are near this level, the data should be interpreted relative to the noise level and in context of other information to determine whether a small amount of water is present in clouds.

2.4.5 Pyranometer, Pyrgeometer, and Pyrheliometer

The downwelling global irradiances in the solar shortwave (0.28-2.8 μm) and thermal longwave (4.0-50.0 μm) were continuously measured with an Eppley pyranometer and pyrgeometer, respectively. Supporting measurements of the direct solar irradiance over the same shortwave band were also continuously obtained with an Eppley pyrheliometer. Measurement precision for these instruments, during CLARET, was better than ± 1.0%, except during and immediately following precipitation events.

These radiometers were mounted on a high point, 5 m above the ground, in the immediate vicinity of lidars and radar. Operation was continuous, with 1/2 Hz sampling and recording of 5-min averages and standard deviations of voltages and resistances. These were later converted to irradiances. The instruments' operation, orientation, and cleanliness were examined frequently by project personnel.

The data set is composed of 5-minute averages of total shortwave irradiance, total IR irradiance, and direct solar irradiance, all in watts per square meter. Examples from October 4 are shown in Figs. 6-8.

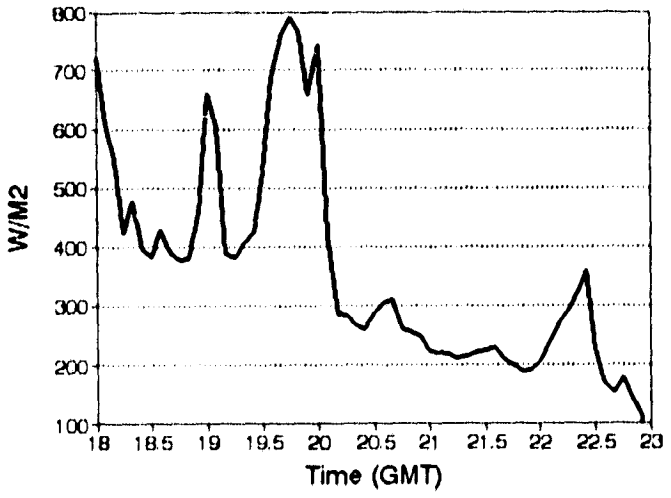

Fig. 6. Pyranometer measurements of downwelling solar radiation on October 4.

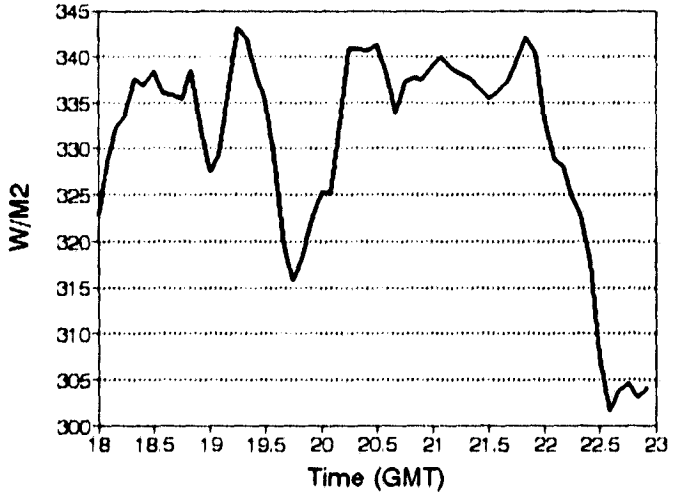

Fig. 7. Pyrgeometer measurements of downwelling infrared radiation on October 4.

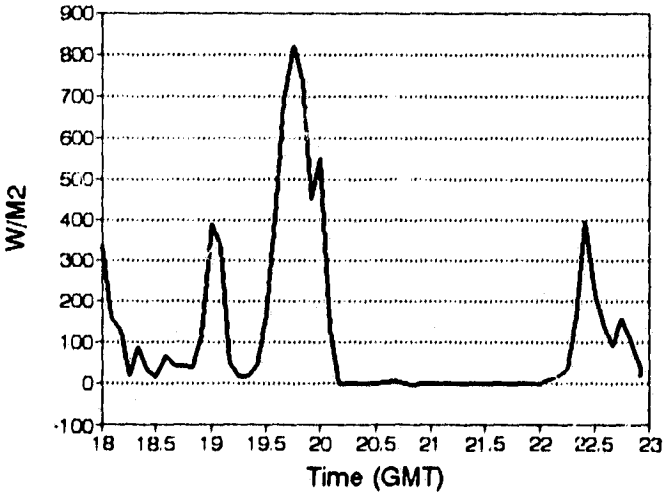

Fig. 8. Pyrheliometer observations of direct solar irradiance reaching the BAO site on October 4.

2.4.6 Narrow-beam Infrared Radiometer

The IR radiometer is a modified Barnes model PRT-5 with a passband covering 9.95-11.43 μm wavelength and 2° field of view. The radiometer was located beside the microwave radiometer at the BAO and was aimed at the zenith. The IR radiometer at SA operated unattended and continuously, but the data were later discovered to be faulty because of calibration problems. An IR radiometer provides an important measurement for understanding the effect of clouds on the thermal radiative transfer. The brightness temperature detected by the IR radiometer indicates cloud presence, and, when combined with temperature profile data, even the approximate cloud base height of optically thick clouds. Also, the detection of a cloud by the IR radiometer but not by the liquid channel of the microwave radiometer indicates that the cloud must be ice. Conversely, a signature in both radiometer outputs indicates that liquid-bearing or mixed-phase clouds are present.

The example data sets in this project report 30-s averages of IR sky brightness temperatures (°C).

2.4.7 Sky Cameras

Two different kinds of sky cameras operated during intensive episodes of CLARET. One was a standard VHS video camera mounted beside the microwave radiometer antenna at the BAO. It was aimed at the zenith and recorded at regular frame speed with a 30° field of view. The other was an all-sky camera, consisting of a time-lapse 16-mm movie camera fitted with a fish-eye lens. It was also located near the radar and lidars. The film was converted to VHS for easier perusal but with some degradation of detail.

Pictures from the all-sky camera provided a means to review the general characteristics of the cloud field for the text summary of each case. In addition, the percentages of cloud cover for averaging periods of 30 min (usually) were estimated from the film and archived with each example data set.

2.4.8 Ceilometer

WPL established a communications link with the Denver NWS to download data from the ceilometer at SA. This instrument is an automated, eyesafe lidar using a laser diode as transmitter. The ceilometer measures cloud base heights (in feet) up to a maximum of 3.7 km AGL. It also reports a thickness measurement, which is analogous to the penetration depth obtained from WPL's research lidar data. The algorithms for determining these parameters are proprietary. The device can obtain these parameters for two or even more layers if partial cover in the lower layers allows an adequate view of higher layers.

Ceilometer data from the stratus case are included in the archive. The ceilometer detected no clouds in the other example cases, presumably because the clouds remained above the ceilometer's maximum height.

2.4.9 Wind Profilers and RASS

Wind profilers are extremely sensitive radars capable of detecting scatter from refractive index inhomogeneities in the clear air. They use the Doppler shift of signals from two or more beams tilted off vertical in different azimuth directions to determine the vertical profile of the horizontal wind. A vertical beam can be used to improve accuracy in precipitation for the shorter wavelengths that also detect these targets. Frisch et al. (1986) described the typical performance of the 50 MHz profiler at the Platteville site and the 915 MHz profiler at SA.

A Radio Acoustic Sounding System (RASS) uses an acoustic source in conjunction with the vertical beam of the wind profiler to measure the speed of sound, from which the virtual temperature is derived as a function of height. May et al. (1988, 1989) described the accuracy and height coverage achievable with this technique. Only the Platteville RASS succeeded in temperature profiling during CLARET I, and then only during September.

2.4.10 Radiosondes

Standard NWS data were collected from the Denver radiosonde, launched from SA. Transmission of the digital values to us failed for some of the profiles, but hard-copy graphs of some of these were available from a different source and are reproduced in Section 3 (Figs. 10-12). For most of the example data sets, tables of vertical profiles of wind, temperature, dewpoint, and pressure are tabulated for the radiosondes launched at the two times that bracket the period of interest.

2.4.11 Surface Meteorological Data

Meteorological data were collected from the 20-m level on the BAO tower for the duration of CLARET. The 20-min averages of wind speed (m s^{-1}) and direction (°), temperature (°C), dewpoint temperature (°C), and barometric pressure (mb) were recorded and are reported for the example cases.

The development of the stratus clouds in the October 3 case depended heavily on the boundary layer meteorology. For this case, we obtained data from a network of 22 surface stations (Fig. 9 and Appendix B) operated by the Forecast Systems Laboratory (FSL) of ERL, except data from the Brighton station are missing. The FSL Mesonet is an experimental

system set up for research purposes. Although every effort is made to maintain the mesonet sensors, measurements may sometimes be in error. Data are reported here in 5-min averages exactly as supplied by FSL's automated system.

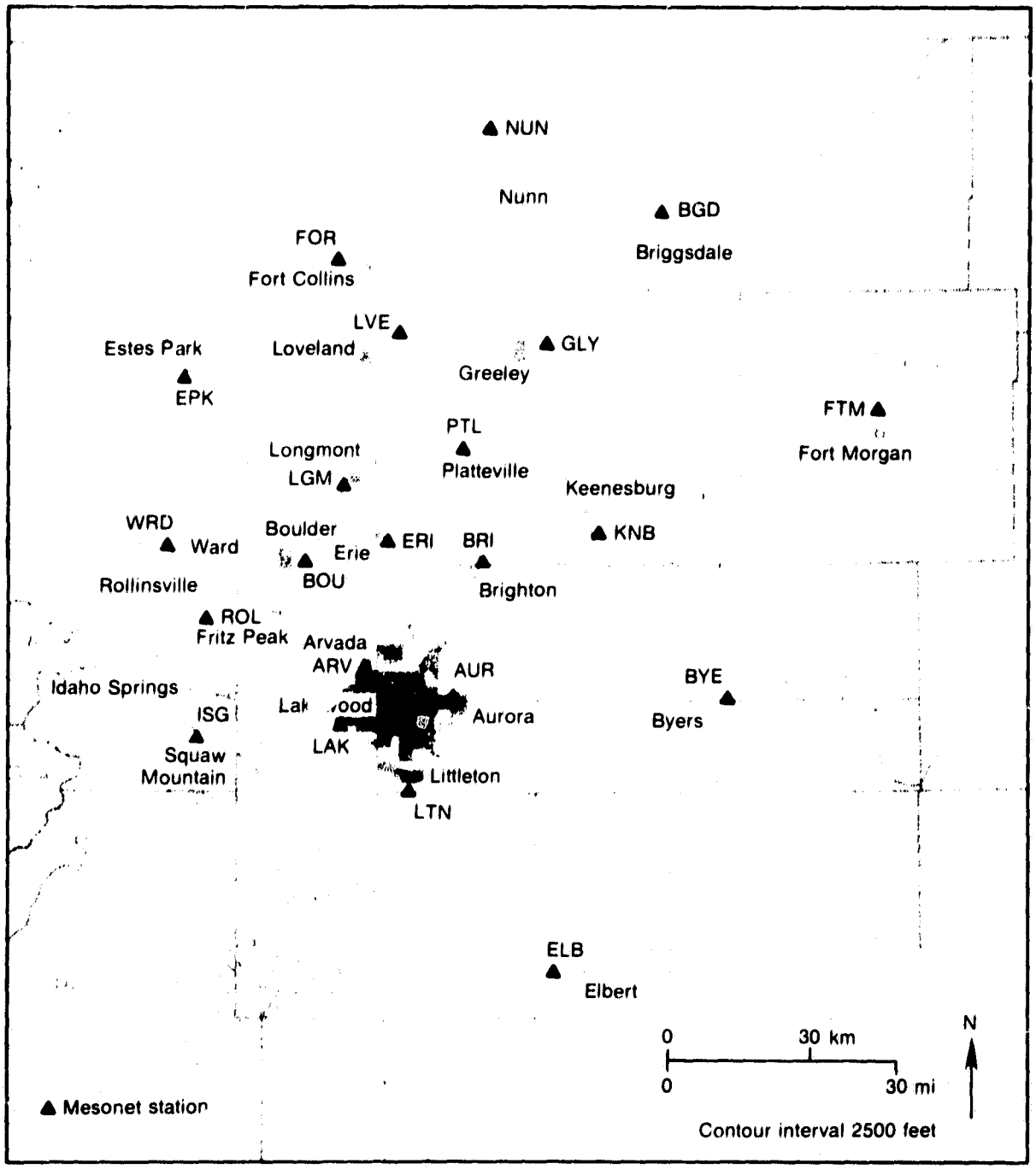

Fig. 9. FSL surface mesonet. See Appendix B for exact station latitude and longitude.

Temperature (°F) was measured in the FSL mesonet by an aspirated thermistor in a standard meteorological instrument shelter, which was usually about 2.5 m above the surface. Dewpoint (°F) was calculated from the relative humidity measurements of a Rotronic YA-100-Hygromer hygrometer, also in the shelter. A propeller vane anemometer measured the wind speed (m s^{-1}) and direction (°) at a height of usually 10 m above the surface. A plastic tipping-bucket measured the 5-min accumulation of precipitation (in). Barometric pressure (mb) was usually measured from within the electronics hut. Each site also had two pyranometer-like instruments using a photovoltaic cell as detector and a translucent plastic diffuser disk to approximate cosine response to solar radiation (W m^{-2}). One instrument was pointed at the zenith in the usual pyranometer configuration. The other was tilted 40° off zenith toward the south and fitted with an artificial horizon to shield the sensor from reflections from the ground.

Appendix B lists some important local characteristics of the instrument sites in the mesonet. Included in the information are a few important exceptions to the normal configuration, e.g., instruments mounted on the roof of a six-story building at the Boulder site.

The example data sets also include the Denver NWS aviation weather reports obtained at SA.

2.4.12 Satellite Radiometers

Synoptic scale and local cloud coverage were provided by satellite data gathered during the experiment. These data provide information about cloud types, moisture sources, and spatial extent of the clouds. The polar orbiter satellites (NOAA 10 and 11) provided two instrument packages. The Advanced Very High Resolution Radiometer (AVHRR) has up to 5 channels (wavelengths of 630 μm, 850 μm, 3.7 μm, 10.8 μm, and 11.9 μm) scanning a swath over 2000 km wide with a resolution of approximately 1 km at nadir. The TIROS Operational Vertical Sounder (TOVS) has three subsystems: the High-resolution Infrared Radiation Sounder mod.2 (HIRS/2), the Stratospheric Sounding Unit (SSU), and the Microwave Sounding Unit (MSU). The HIRS/2 measures incident radiation in 19 regions of the IR spectrum and 1 region of the visible spectrum. The SSU has 3 channels at 15 μm. The MSU is a 4-channel Dicke radiometer making passive measurements in the 5.5 μm oxygen band. The TOVS provides approximately 50 km resolution over the scanning swath. Data from NOAA 10 and 11 were received twice per day from each satellite. More frequent cloud observations were provided by the Geostationary Operational Environmental Satellite (GOES). Hourly data were collected from the 6.73 μm, 11.24 μm, and 12.66 μm channels. The GOES radiometers provided continent-wide coverage at 8-km resolution.

An example of cloud cover and top height information was obtained from an image created using NOAA 10 AVHRR channel 4 (10.8 μm) data from a pass at 1430 UTC on September 28. The image (512 km × 512 km) was centered on the BAO. Much of the image was cloud-free and clearly revealed the North Platte River in southwestern Nebraska and the Arkansas River in southeastern Colorado. Using these two prominent features, the image was fine-scale navigated to within 1 km.

A 100-km × 100-km subsection of the image was selected for analysis. The center of this section was located 25 km to the east of the BAO in order to avoid mountain topographic effects. The southeast part of this section was dominated by cloud-free pixels. The western half of the section was dominated by cold brightness temperatures (high clouds). In the transition areas between these two regions, there was a distinct layer of low-level clouds. A histogram of the pixel temperatures in this 10^4 km^2 section shows that approximately 30% of the pixels were centered on 14°C, indicating cloud-free areas. The dominant brightness temperature of the low-level clouds was 10°C, with a cutoff temperature of 2°C. The coldest temperature in this image subsection was -32°C, and the warmest temperature was 17°C.

The image subsection was further broken down into 100 minisections, 10 km × 10 km, and histograms of pixel temperatures were determined for each minisection. A summary of the resultant temperature distributions is given in Tables 3-5. Table 3 shows the number of cells in which the surface is visible (temperatures greater than 10°C) as a percentage of the total number of cells in the minisection. The star symbol locates the position of the BAO; north is up and east is to the right in Tables 3-5. A dash means 0%. Table 4 shows the number of cells that indicate the presence of low clouds (temperatures less than 10°C but greater than 2°C). Table 5 shows the number of cells where only high clouds can be detected (temperatures less than 2°C).

A previous study (Derr et al. 1990) demonstrated that the 11.24 μm GOES brightness temperature estimates of cloud top temperature agreed to within 1°C of the physical temperature estimated using radiosonde data. This method was used to estimate cloud top heights for the October 3 stratus case (Section 3.4).

3. DATA FORMATS AND SYNOPSES OF CLARET CASES

After discussion with scientists at Los Alamos Scientific Laboratory, WPL selected five cases for the example data sets that represent different cloud conditions. Three cases involved cirrus observations. Two of the cases, one a stratus and the other a clear case, had cloud conditions that were not the primary focus of CLARET, but they satisfy the research interests of certain Los Alamos scientists and are valuable for development of the ARM program.

This section first describes the data formats. Then the cloud conditions, the synoptic meteorology, and the data availability are summarized for each case.

Table 3. Percent of area free of clouds in 100 cells of area 100 km^2 as inferred from AVHRR brightness temperatures at 1430 UTC on September 28

2.48	14.88	4.13	25.62	17.36	9.09	38.02	73.55	87.60	52.89
-	-	5.13	7.44	15.70	-	-	-	6.61	27.27
1.65	18.18	4.96	0.83	53.72	67.77	68.10	0.83	-	-
-	-	-	1.65	11.57	49.59	70.25	70.25	53.72	18.18
0.83	-	0.83 ★	4.96	16.53	56.20	58.68	52.89	44.63	94.21
8.26	0.83	1.65	-	-	20.66	57.02	80.99	95.04	100.00
1.65	4.13	4.96	3.31	-	-	7.44	16.53	85.12	67.77
-	0.83	3.31	13.22	11.57	3.31	12.40	22.31	71.51	52.07
4.13	0.83	12.40	2.48	18.18	35.54	34.71	79.34	82.64	69.42
-	3.31	-	0.83	25.62	83.47	63.64	95.04	89.26	90.08

Table 4. Percent of area with low clouds for same cells as in Table 3

4.96	13.22	36.37	32.23	38.84	70.25	48.76	19.84	12.40	31.41
15.70	16.53	46.28	50.41	18.18	16.53	42.15	19.01	19.01	33.06
27.28	46.28	33.88	33.05	39.69	23.97	19.01	9.09	8.26	16.53
-	3.31	58.68	47.94	38.84	19.01	27.27	20.66	31.40	12.40
16.53	13.22	14.05	48.76	75.21	42.15	23.14	38.02	44.63	5.79
30.58	26.44	8.27	9.40	18.64	38.84	31.41	19.01	4.96	-
19.01	42.15	32.23	39.67	23.14	17.36	31.40	40.49	14.88	29.75
9.09	9.09	11.57	18.18	30.58	16.52	24.79	44.63	27.28	43.80
24.80	20.66	19.83	14.88	46.28	39.67	48.76	18.18	16.53	28.10
21.49	17.35	18.18	29.75	40.50	13.22	35.53	4.96	10.74	9.92

Table 5. Percent of area with high clouds for same cells as in Tables 3 and 4

92.56	71.90	59.50	42.15	46.80	20.66	13.22	6.61	-	15.70
84.30	83.47	49.59	42.15	66.12	73.47	57.85	80.99	74.38	39.67
71.07	35.54	61.16	66.12	6.61	8.26	52.89	90.08	91.74	83.47
100.00	96.69	41.32	50.41	49.59	31.40	2.48	9.09	14.88	69.42
82.64	86.78	85.12	46.28	8.26	1.65	18.18	9.09	10.74	-
61.16	72.73	90.08	90.60	81.36	40.50	11.57	-	-	-
79.34	53.72	62.81	57.02	76.86	82.64	61.16	42.98	-	2.48
90.91	90.08	85.12	68.60	57.85	80.17	62.81	33.06	1.65	4.13
71.07	78.51	67.77	82.64	35.54	24.79	16.53	2.48	0.83	2.48
78.51	79.34	81.82	69.42	33.88	3.31	0.83	-	-	-

3.1 Data Formats

Tabulations of the archived data are available on IBM-compatible diskettes, which can be obtained by contacting either of the following:

Dr. Wynn L. Eberhard
R/E/WP2
NOAA Wave Propagation Laboratory
U.S. Dept. of Commerce
325 Broadway
Boulder, Colorado 80303

Telephone: (303) 497-6560
FAX: (303) 497-5318

Dr. Paul Mutschlecner
EES-5
Los Alamos National Laboratory
Los Alamos, New Mexico 87545

Telephone: (505) 667-8063
FAX: (505) 665-3687

The data are available on IBM-compatible diskettes in ASCII format. Each case is in a different directory. Measurements are tabulated according to time UTC (= MST + 7 h) and grouped within files according to parameters or instrument. Table 6 lists these parameters and serves as a table of contents for the data on diskette. As can be seen from the table, the files are named according to parameters (e.g., RADIATN), instruments (e.g., MESONET), or both (e.g., CLDHTCO2). The extension with each file name (e.g., 271 in CLDHTRUB.271) gives the day number of the case. Documentation at the head of each file, supported by the additional information in this report, should completely explain the data.

3.2 Cirrus, 1400-1630 UTC on Day 271 (September 28)

A low-pressure center off the coast of California was still blocked by a high-pressure ridge over the southwest United States. To the north of these stalled systems, a trough axis followed by a cold front was moving slowly southeastward and creating the cloudiness over northeastern Colorado. The synoptic situation had persisted with little change for 3 days.

The clouds over the BAO during this intensive period were mostly high clouds situated within the zone of approximately 6-8 km AGL. They initially were cirrocumulus clouds that diminished in optical thickness with time, giving way to cirrus fibratus and cirrus uncinus after 1540 UTC. Only scattered clouds remained by 1630 UTC. The clouds were organized somewhat into bands, with many smaller cloud elements in each band. The bands were aligned slightly off the westerly wind direction, with first the northern and later the southern edge of each band slipping over the BAO as the clouds advected with the wind. Visual and satellite observations showed that the clouds formed far upwind of the Continental Divide.

Table 6. Directory giving the timespan of data on diskettes and in this report

Parameters	File Name	Sept. 28 Day 271	Sept. 30 Day 273	Oct. 3 Day 276	Oct. 4 Day 277	Oct. 5 Day 278
Nominal period (UTC)		1400-1630	1450/1700	1200-2130	1900-2120	1415/1615
Cloud conditions		Cirrus	Clear	Stratus	Mixed	Cirrus
Cloud heights						
Ruby lidar	CLDHTRUB	1350/1619		1546/2109	1855-2118	1415-1615
CO_2 lidar	CLDHTCO2	1421/1749			1927/2120	
Ceilometer	CLDHTCEL			1100-2030		
Radar	MWAVE&IR	1400-1630		1200-1915*	1904/2128	1415-1615
Percent cloud cover						
All-sky camera	COVERCAM	1400-1630	1450-1700	1540/2140	1900-2100	1415-1530
BAO observer	COVERBAO	1405/1713		1553/2115	1932/2128	1417/1516
Satellite AVHRR	COVRSATh	1430				
Aviation weather reports						
Stapleton Airport	NWSDENWX	1351/1651	1352/1751	0750/2151	1851/2151	1350/1650
Radiation						
Global star	RADIATN	1400-1800	1450-1700	0800-2130	1800-2300	1410-1700
Global IR	RADIATN	1400-1800	1450-1700	0800-2130	1800-2300	1410-1700
Direct solar	RADIATN	1400-1800	1450-1700	0800-2130	1800-2300	1410-1700
Narrow-beam IR	MWAVE&IR	1400-1630		1604-2130	1904/2128	1415/1615
Surface meteorology						
BAO	METBAO	0000-1440	0000-2400	1420-2400	0000-2400	0000-1440
FSL mesonet	MESONET			0000-2400		

(continued on next page)

Table 6. (continued)

Parameters	File Name	Sept. 28 Day 271	Sept. 30 Day 273	Oct. 3 Day 276	Oct. 4 Day 277	Oct. 5 Day 278
Temperature soundings						
Radiosonde	TEMPSOND	1100/2300	1100/2300	1100/2300	1100/2300	1100*/2300*
RASS	TEMPRASS	0052/2352	0052-2252			
Wind soundings						
Radiosonde	WINDSOND	1100/2300	1100/2300	1100/2300	1100/2300*	1100*/2300*
Denver profiler	WINDDENP	0000/2400	0000-2400	1200-2000	1900-2140	1400-1620
Platteville profiler	WINDPLTP	0000-2200	0000-2400	1248-1937		1356/1658
Water soundings						
Radiosonde dewpoint	TEMPSOND	1100/2300	1100/2300	1100/2300	1100/2300	1100*/2300*
Integrated vapor	MWAVE&IR	1400/1630	1430-1730*	1604-2130	1904/2128	1405/1615
Integrated liquid	MWAVE&IR	1400/1630		1604/2130	1904/2128	1415/1615
Integrated ice	MWAVE&IR	1400-1630			1904/2128	1415-1615
Aerosol backscatter@	AERdtttt	1451/1709				

- Data essentially continuous
/ Data set has significant gaps
* Data in text instead of on diskette
@ See text for explanation of files

These high clouds were composed mostly of ice, as determined from ruby lidar depolarization and microwave radiometer data. The microwave radiometer observed no detectable water. The ruby lidar depolarization ratio was small in some patches and layers of the clouds. However, data from the ruby lidar when it rocked about zenith during the period 1520-1530 UTC and backscatter intensity data at other times suggest that most of these low-depolarization parts contained oriented crystals. The possibility exists, however, that some very small fraction of the cloud volume may have contained water.

During the first 5 min of the period (until 1405 UTC), the ruby lidar detected a layer of liquid cloud at 4 km AGL while penetrating to observe the higher cloud. This was the last remnant of an episode of thicker middle clouds observed by the IR and microwave radiometers for a time preceding 1400 UTC.

AVHRR data at 1430 UTC (Section 2.4.12) showed both high and low clouds in the vicinity of the BAO, which is consistent with surface-based observations of low clouds disappearing first and high clouds thinning out later. The data in Tables 3-5 are in diskette files named COVERSTh, where *h* is S, L, or H, meaning surface, low clouds, or high clouds, respectively.

The radar detected only part of the clouds observed by the lidar. The radar observed neither the water cloud (4 km AGL) nor the cirrocumulus (7-8 km AGL) during 1400-1430 UTC. It detected only the densest parts of the cirrus fibratus and uncinus clouds after 1530 UTC. The cirrus clouds had a complicated structure with wide variations in optical depth, as inferred from large variations in sky brightness temperature, surface solar measurements, and lidar and radar backscatter.

The SA ceilometer observed no clouds within its range during this period, so no file of null data was included in the archive.

3.3 Clear Skies, 1450-1700 UTC on Day 273 (September 30)

Colorado was under high pressure. The skies over the BAO were clear during this period, although small cumulus clouds formed and evaporated over the mountains a far distance to the west. Aerosol particles were noticeable in the planetary boundary layer, but they did not form a strong haze. The ruby lidar revealed that an aerosol layer extended rather uniformly to 3 km AGL and indicated that very little aerosol was present at greater tropospheric heights. The mixed layer this early in the day could not be expected to be as deep as this aerosol layer, which apparently developed from earlier mixing processes.

The ruby lidar performed a few horizontal and vertical measurements, from which optical information on the haze layer was extracted. The extinction coefficient (molecular plus aerosol) within the mixed layer was found by aiming near horizontal and determining the decrease with range of the measured backscatter. This method assumes horizontal

homogeneity of the aerosol over the path of the lidar pulse. These data were acquired while scanning the lidar from local horizon to 1 or 2° elevation angle in an attempt to average out some of the aerosol variability. This case complied with the condition of aerosol homogeneity only to a fair degree, so rather large error bars must be assigned to the estimate of extinction coefficient. Our result was $4.7 \times 10^{-5} \pm 1.0 \times 10^{-5}$ m^{-1}. Assuming a constant extinction coefficient from the surface to 3 km AGL, the optical depth of this layer at 0.7-μm wavelength was estimated as 0.14. The lidar was calibrated by assuming molecular scatter in the free atmosphere where the vertical profile of lidar signal indicated no aerosol structure.

Range-resolved lidar profiles of apparent backscatter coefficient (uncorrected for atmospheric attenuation) are recorded on diskette in files named AERdtttt.273. The d refers to the direction of aim, namely H for horizontal and V for vertical. The time (UTC) of measurement is listed in the place of tttt.

The computer which recorded the data from the microwave and IR radiometers at the BAO failed on this day. As a substitute to aid in radiative transfer calculations, the precipitable water data from the microwave radiometer at SA are listed in Table 7.

Table 7. Column-integrated water vapor at SA on September 30

Begin time (UTC)	Column-integrated Water vapor (cm)
1430	1.12
1445	1.11
1500	1.11
1515	1.12
1530	1.15
1545	1.18
1600	1.13
1615	1.11
1630	1.10
1645	1.08
1700	1.07
1715	1.07

3.4 Stratus, 1200-2130 UTC on Day 276 (October 3)

A low-pressure system was centered over the intersection of the Utah, Idaho, and Nevada state lines, and a ridge axis extended from Oklahoma through Kansas and to the Dakotas. A short wave passed through Colorado, causing an event of low clouds and stratus in the Denver-Boulder-Longmont region just east of the Rocky Mountains. Orographic lifting of the flow over the plains contributed to cloud formation; the plains slope gently downhill from the foothills in a direction approximately toward the northeast. The period 1200-2130 UTC began with the development of the cloud system and ended with the completion of the dissipation phase.

The winds advecting the clouds turned from west northwest through north to northeast as time progressed in this period. Starting at 2030 UTC, the all-sky camera at the BAO showed an increasing number of the clouds persisting locally for 5-15 min, as if tied to nonpropagating updrafts in the boundary layer.

The depolarization signature of the ruby lidar showed only a water phase in the clouds it detected during this event, although it operated only a total of 3 h 20 min. During those times, it measured base heights between 700 and 950 m AGL and penetration depths of 200 m or less. The time-height displays of the lidar backscatter gave every indication of complete attenuation before reaching cloud top. The ceilometer at SA obtained similar cloud base heights, but lesser penetration depths and occasionally a second layer 100-200 m higher. The radar sometimes observed weak signals during part of the period, which could be interpreted as cloud within the zone 1.5-3.7 km AGL. This is one illustration of the complementary role of radar and lidar, which detected different parts of the cloud.

The only satellite data available for this period were from GOES. The brightness temperatures in the 11.24-μm wavelength channel were examined to obtain cloud top temperatures. At 1500 UTC, the stratus layer was limited to the area east of the Rocky Mountains. The cloud top temperatures within 40 km of the BAO were quite uniform at -2°C. Succeeding GOES images showed the eastern edge of the stratus receding toward the west. At 1800 UTC, the layer extended only 25 km to the east and south of the BAO, still with cloud top temperatures of about -2°C. This cloud top temperature is consistent with the highest cloud signal detected by the radar at 3.7 km AGL.

The drops in the stratus cloud were too small in size and number to be clearly detected by the radar. Our software for determining cloud boundaries from the radar data was not successful. However, some information on cloud heights was gleaned from time-height diagrams of radar data and is summarized as follows:

1200-1300 UTC (monitoring mode): The radar detected boundary layer targets from the surface up to about 2 km AGL. These targets were probably insects or organic debris carried by the winds.

1300-1520 UTC (monitoring mode): The radar continued to detect boundary layer targets from the surface up to about 2 km AGL. In addition, a stratus cloud lay above the boundary layer between 1300 and 1430 UTC. The radar-detected cloud was generally situated between 2.2 and 2.5 km AGL, and never exceeded 0.5 km in thickness.

1520-1835 UTC (monitoring mode): The radar continued to detect boundary layer targets from the surface up to about 2 km AGL. A stratus cloud moved into view at about 1520 UTC and thickened as time progressed until about 1835 UTC. It began with a thin layer at 2.7 km AGL and spread into a 2.2-km-deep layer centered at about 2.7 km AGL.

1835-1915 UTC (intensive mode): The cloudiness persisted, but with very weak radar signal, having a thickness of about 1.5-2 km, centered at about 2.6 km AGL. The radar-detected cloud appeared to have a broken rather than a stratus structure, and an intermittent double-layered structure was suggested.

3.5 Mixed-Phase Clouds, 1900-2120 UTC on Day 277 (October 4)

The 1200 UTC weather maps show a mid-level low centered over central Montana with its associated surface low in southern Wyoming. Trailing off this low was a cold front extending southeastward through western Colorado and reaching to southwestern Arizona. Tropical storm Raymond, recently downgraded from a hurricane, was off the coast of Baja. Moisture was riding into Colorado on the subtropical jet from the southwest. By 1800 UTC, the trough axis had moved southeastward and was situated over eastern Colorado. The surface low with its connecting fronts was situated over southeastern Colorado. Numerous showers and thundershowers were occurring over eastern Arizona, over western New Mexico, and along the east side of the Rocky Mountains in southern Colorado. Cloudy skies prevailed over much of Colorado for this intensive period.

Visual observations from the BAO during the intensive period revealed a variety of cloud types in the area, namely altocumulus, altocumulus undulatus, altostratus, cirrostratus, and wave clouds near the mountains. The lidars and radar observed clouds within the zone 3.5-7 km AGL. The ruby lidar's backscatter showed two or more connected layers most of the time. One exception was between 1946 and 2006 UTC, when at least one of the layers was separated from the others by clear air. A thin layer that strongly attenuated the lidar signals was overhead for 2.5 min starting at about 20:56:30 UTC. The bulk structure of the clouds during this 2.5-h period was very complex, and the details changed considerably as the clouds advected over the BAO.

The distribution of microphysical structure in this case was also complicated. The microwave radiometer at the BAO measured varying amounts of liquid water. Local peaks in liquid water were observed at 1915, 2020, and 2100 UTC. No liquid water was detected from (approximately) 1900 until 1907, from 1935 until 2007, and at 2035 UTC. The columnar liquid water varied erratically from one 30-s sample to the next from about 2100 UTC onward. The ruby lidar scanned near zenith for almost this entire period. Most of the time, depolarization was small within one or more layers of the cloud and strong in other parts of the cloud. Unfortunately, we failed to scan far enough off vertical to discriminate unequivocally between water or enhanced backscatter when depolarization was small. However, the microwave radiometer and ruby lidar data taken together suggest that liquid water was sometimes present in ice-free layers and at other times within the same layer as oriented crystals.

Transmission of the digital values for the wind data from the 2300 UTC radiosonde profile was unsuccessful, but approximate values can be obtained from Fig. 10.

3.6 Cirrus, 1415-1615 UTC on Day 278 (October 5)

Raymond, recently downgraded to a tropical depression, was centered over Arizona, and a low-pressure area was situated over northern Minnesota. Raymond was the source of moisture for a band of cloudy weather roughly the width of Colorado; it extended northeast from Arizona, past eastern Colorado, and on toward Lake Superior. The 1535 UTC national radar summary from NWS showed several light rain showers over extreme eastern Colorado. From the BAO, we visually observed blue sky at the horizon far to the west and cirrocumulus and cirrostratus at large distances to the south and east.

Cirrus fibratus within a height zone of about 7.5-9 km AGL initially prevailed over the BAO, thinning out as time progressed, until about 1525 UTC. This was replaced by a system of cirrocumulus, arranged in cross-wind rolls, that increased from a sparse to a concentrated field. The maximum geometrical thickness passed overhead at 1553 UTC, and then the field gradually faded to a few thin patches. The cirrocumulus clouds occupied the zone 7.7-10 km AGL. The ruby lidar and microwave radiometer indicated that the cloud consisted entirely of ice particles.

The radar was unable to detect the cirrus much of the time, and then only some pieces near 8 km AGL. The total backscatter measured by the ruby lidar generally tracked well the brightness temperature measured by the IR radiometer.

The radiosonde data for this case are shown in Figs. 11 and 12, because transmission of the digital values to us was unsuccessful.

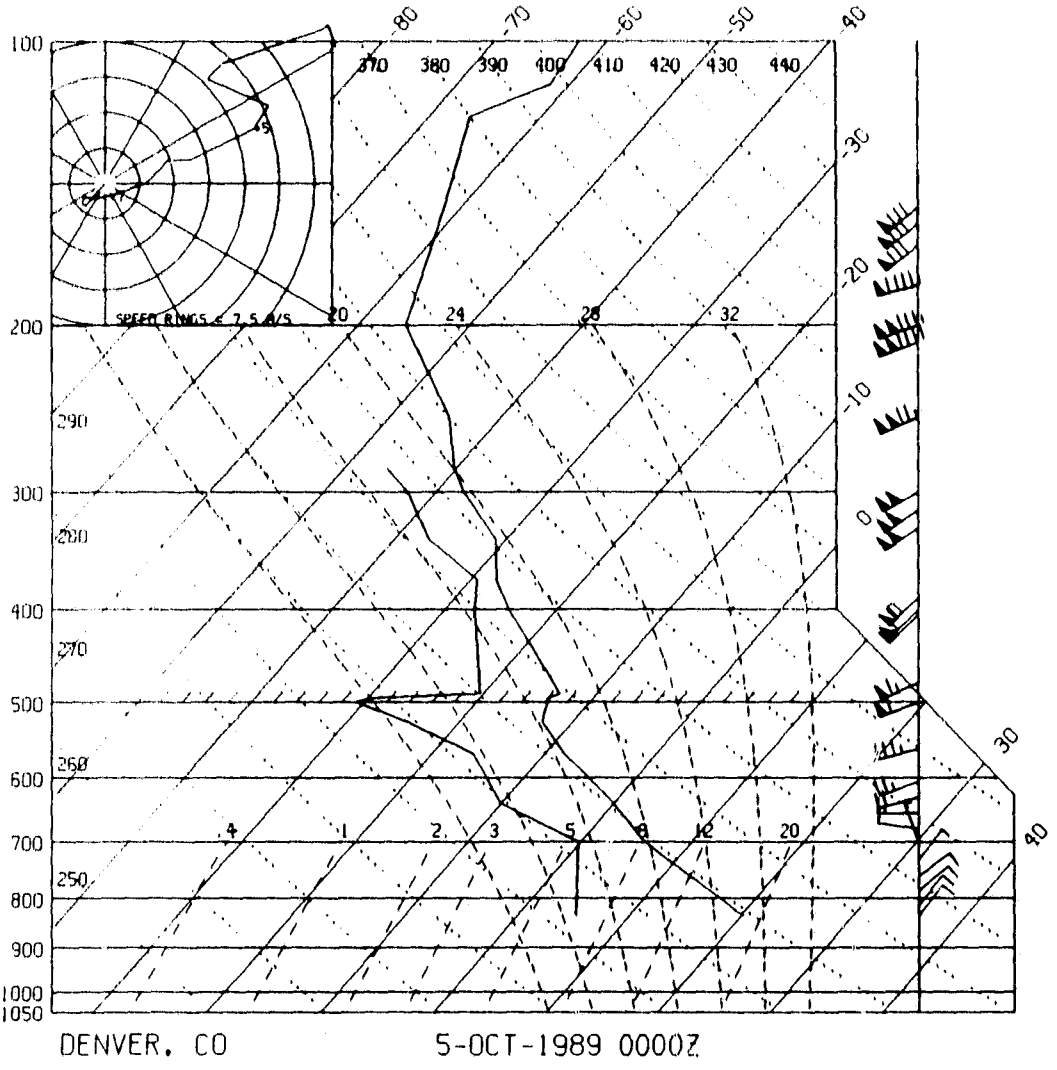

Fig. 10. Temperature, dewpoint, and wind profiles at about 2400 UTC on October 4 from a NWS radiosonde launched from SA. Data are plotted on a skew-T diagram, and wind barbs are 5, 10, and 50 knots for a half, full, and triangular barb, respectively.

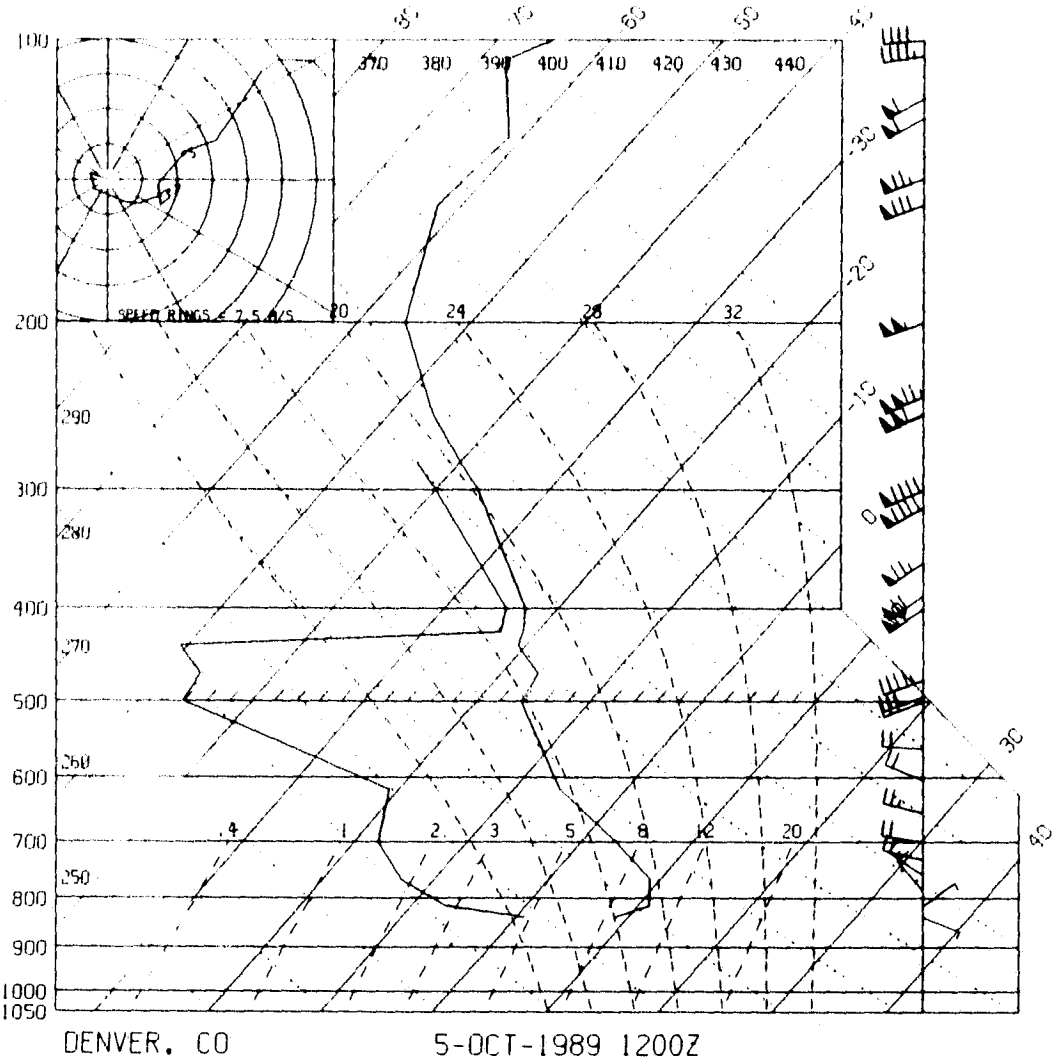

Fig. 11. Temperature, dewpoint, and wind profiles as in Fig. 10, except for 1200 UTC on October 5.

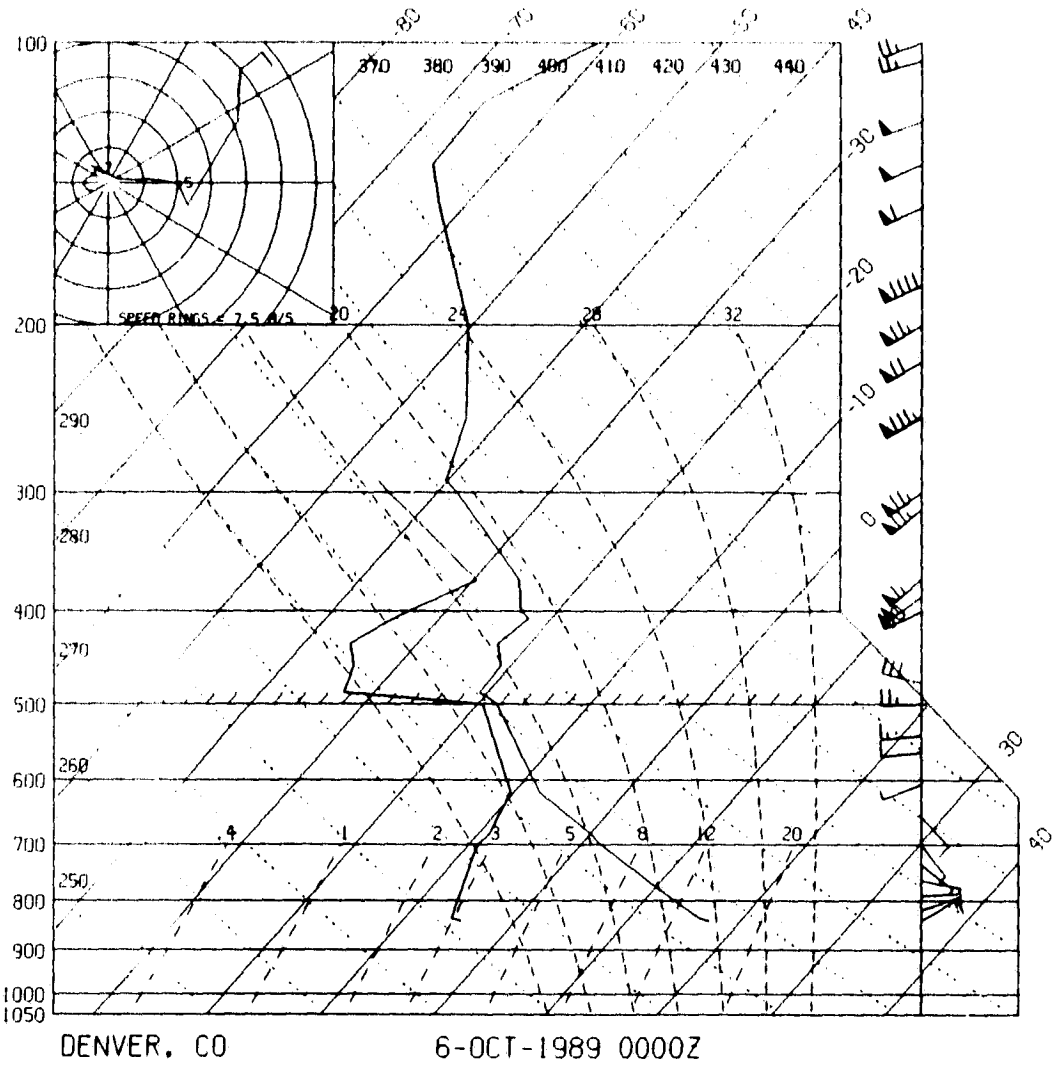

Fig. 12. Temperature, dewpoint, and wind profiles as in Fig. 10, except for 2400 UTC on October 5.

4. PRELIMINARY RESULTS OF TECHNIQUE RESEARCH

This section describes several WPL research endeavors for developing new cloud-sensing techniques. Some of the examples use CLARET data. All the techniques could be valuable components of CART measurements.

4.1 Lidar-Radar Estimates of Effective Radius of Ice Particles

The following description briefly outlines the method used to derive cirrus particle size from simultaneous ground-based IR lidar and microwave radar backscatter measurements (Intrieri et al., 1991). The wavelength difference between these two instruments produces a differential backscatter signature that contains information on the effective size of the scatterers.

Theoretical estimates of the radiation backscattered from a cirrus cloud described by a modified gamma distribution were calculated using Mie scattering theory for both lidar and radar wavelengths. The ratios of the backscatter cross sections (radar/lidar) were compared with the effective radius calculated for the size distributions so that an approximate relationship could be formed between the backscatter ratio and the effective radius. These values were then compared with observed returns to yield estimates of particle effective size. Figure 13 illustrates the theoretical ratios of K_a- and X-band radar backscatter to CO_2 lidar backscatter, each versus effective radius. Two cirrus size distributions with substantially different widths were assumed.

Figure 14 is an example of an effective radius profile produced using this method. Backscatter values from the vertically pointed radar and lidar were matched every 75 m to yield range-resolved cirrus cloud particle size estimates.

In this initial assessment, we assumed the cirrus cloud is composed of spherically shaped ice particles in a modified gamma distribution. Current research is investigating other shapes (cylinders and plates), differently shaped size distributions (e.g., Marshall-Palmer), and estimates of other parameters (e.g., number density of the particles). We are also refining the method to properly account for extinction of lidar radiation by the cloud. The technique will be further assessed using comparisons with aircraft data from the FIRE II [First ISCCP (International Satellite Cloud Climatology Program) Regional Experiment] cirrus experiment, held in November-December 1991. We plan to apply the technique to the large volume of data acquired in that experiment.

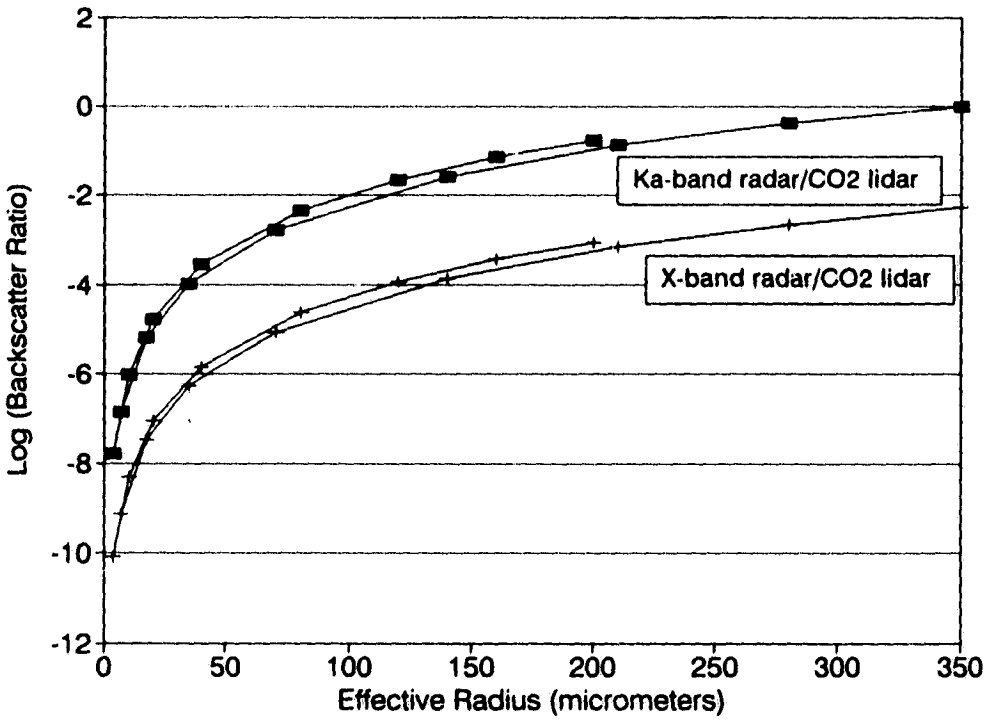

Fig. 13. Theoretical ratios of the backscatter coefficients for the K_a-band radar to those of the CO_2 lidar (filled squares) and the X-band radar (as used in CLARET) to the CO_2 lidar (crosses), versus effective radius. Calculations are for two series of size distributions with proportionately different widths.

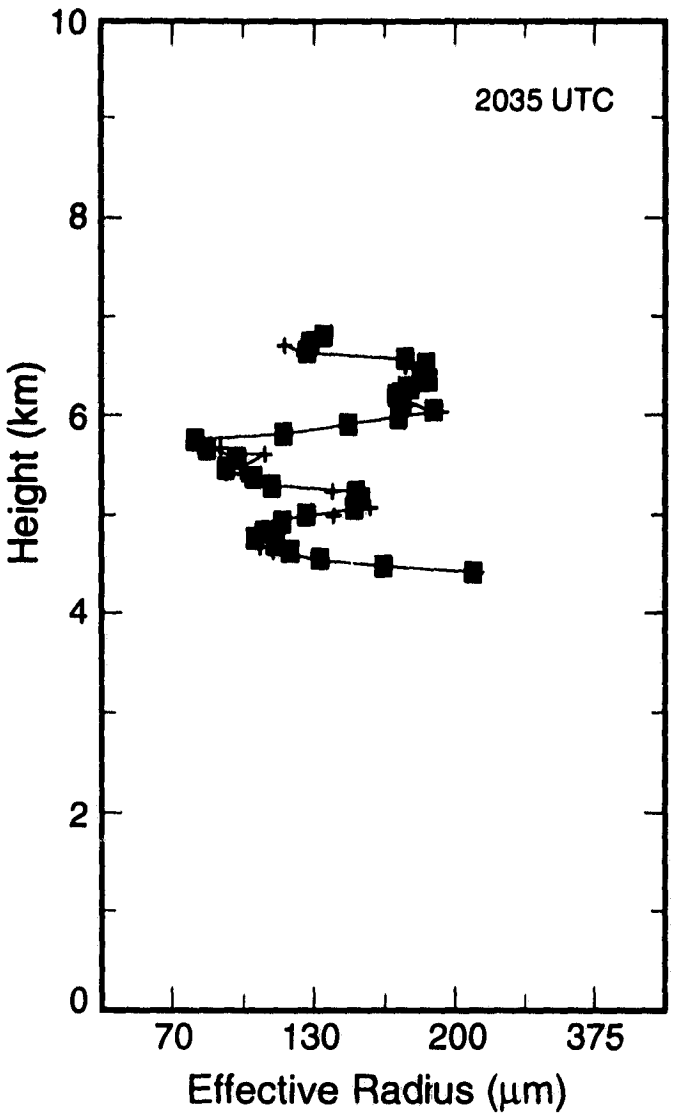

Fig. 14. Vertical profile of the effective radius for 2035 UTC on October 4 using an algorithm derived from Fig. 13. Crosses and squares designate two different profiles with 15 s separation.

4.2 Radar/Infrared Radiometer Estimates of Cloud Microphysics

A technique was developed (Matrosov et al., 1992) to determine characteristic ice particle sizes and concentrations from simultaneous ground-based radar and IR radiometer measurements. The technique is based on the theoretical consideration of the thermal radiative transfer within a cloud and can be applied to clouds that are semitransparent in the IR "window" and horizontally extensive.

It is well known that brightness temperatures T_b of semi-transparent ice clouds depend primarily on their optical thickness τ and the temperature profile. If the temperature profile is known (for example, from radiosonde data), it is possible to obtain from IR radiometer measurements the value of τ. This τ and the radar reflectivity, Z, depend on particle sizes and concentrations, but in different ways. Assuming a shape of the particle size distribution (for example, the modified gamma distribution), it is possible to develop two equations relating Z and τ with two parameters of cloud microstructure, namely, particle concentration C and particle median diameter D_m. Obtaining values of Z and τ from measurements, one can solve these equations and extract values of C and D_m.

Although radar measurements are range resolved, the IR radiometer responds in an integrated fashion to the whole vertical extent of a cloud. Vertically averaged radar reflectivities Z are therefore used, and only values of C and D_m averaged through the cloud's vertical extent can be obtained.

The CLARET data set resulted in an excellent example of a persistent, semitransparent cloud of great horizontal extent on October 4. Between 1900 and 2100 UTC, this cloud also had relatively stable bottom and top heights as detected by the radar (about 4.0 and 6.5 km, respectively; Fig. 3). Using microwave radiometer data as a filter, we were able to extract the time periods when the cloud was composed of only ice particles, avoiding episodes when there were significant amounts of liquid water in the cloud. Figure 15 shows time series of the results from this new technique. Data gaps represent time periods when either liquid water contents exceeded a small threshold value of 0.1 mm or the radar was not collecting data in the vertical mode. The vertically averaged cloud particle median sizes and number concentrations derived from the simultaneous radar and IR measurements are both shown.

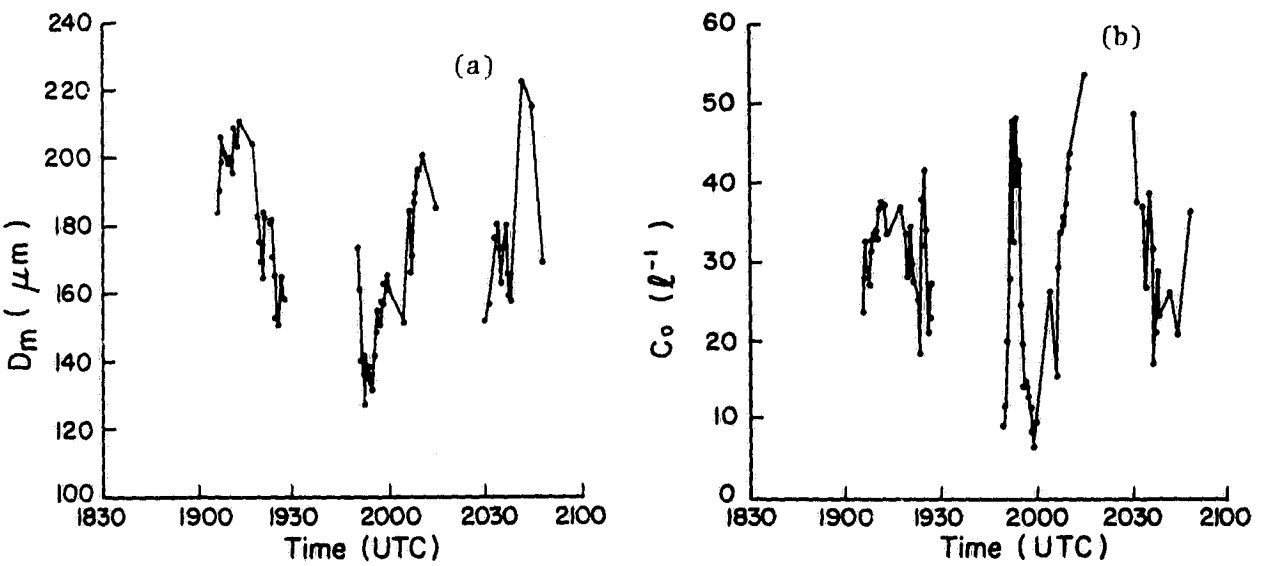

Fig. 15. Time dependencies of (a) retrieved cloud particle median diameter, and (b) concentration, on October 4 using the radar-radiometer method.

4.3 Radar Estimates of Ice Water Content

Sassen (1987) developed an empirical equation relating radar reflectivities to ice water content (IWC). The equation is based on a composite data set on low polar clouds, collected by several researchers. Low polar clouds by virtue of their temperature were considered to be microphysically similar to cirrus clouds, and both IWC and radar reflectivities were calculated from a sampling of crystals collected at the ground. Although this relationship is not unique, it appears that in some cases it gives useful estimates of IWC.

Figure 16 shows ice water path (IWP), which is IWC integrated along the radar beam using Sassen (1987), for the October 4 case. This is plotted against downward brightness temperatures measured by the IR radiometer (with periods of high liquid water content omitted). Periods are excluded when the microwave radiometer observed substantial liquid water content overhead. Although there was only a weak relationship (not shown) between brightness temperature and either cloud base height or cloud thickness (as would be expected from clouds that are optically thin and variable), there appears to be a strikingly good relationship between IWP and brightness temperatures. It can be argued whether IWC can be accurately parameterized by radar reflectivities, but, in this case, the vertically-integrated radar reflectivities are clearly representative of a bulk property of the cloud that is intimately related to the radiative properties of the cloud. This is a promising result, especially in light of the difficulty in relating radiative properties to microphysical properties of the cloud, such as effective radius.

Figure 17 shows a scatter plot of IWP calculated for Sassen's technique and IWP calculated by the method described above (Matrosov et al., 1992), where IWP is based on the derived particle concentrations and effective radius. The two procedures are not completely independent because both use the same radar data. However, the good agreement is encouraging. Both methods will be evaluated for other cases and compared with other techniques for obtaining IWC.

4.4 Ice Cloud Depolarization of CO_2 Lidar Backscatter

Sassen (1991) summarized how depolarization of lidar backscatter can be used to discriminate the water, ice, and mixed phases of clouds. This technique has been used with shortwave lidars, which operate within or near visible wavelengths where the absorption by water and ice is very small. According to usual practice, a pulsed laser transmits linearly polarized light and a receiver detects two linear polarizations, one parallel to that transmitted and the other perpendicular. The linear depolarization ratio δ_l is the ratio of the perpendicular backscatter coefficient to the parallel backscatter coefficient. The δ_l for single backscatter from cloud drops is small, $\approx$0.03, because of the symmetry in the spherical shape of the drops. The highly nonspherical shapes of ice particles cause substantial depolarization in shortwave lidars, such that δ_l from pure ice clouds typically varies over the range from 0.35 to 0.7. A value of 0.15-0.35 for δ_l indicates a mixed-phase cloud when multiple scatter

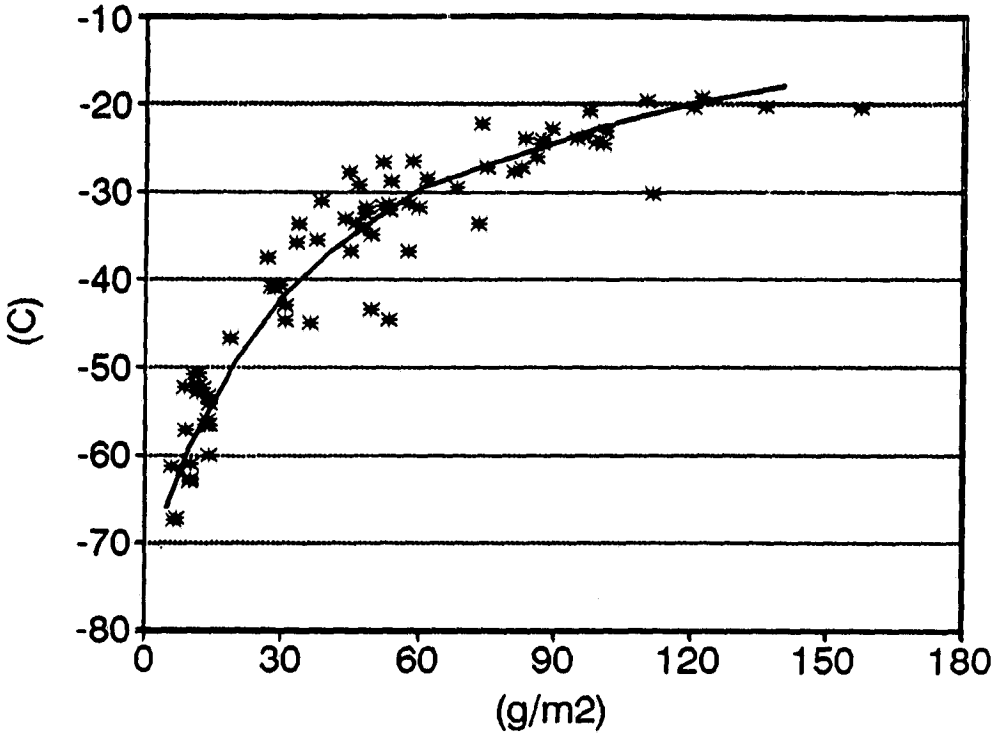

Fig. 16. Ice water path from the method of Sassen (1987) compared with the brightness temperature measured by the IR radiometer for the October 4 case. The line shows estimates from the method of Matrosov et al. (1992) for D_m = 170 μm.

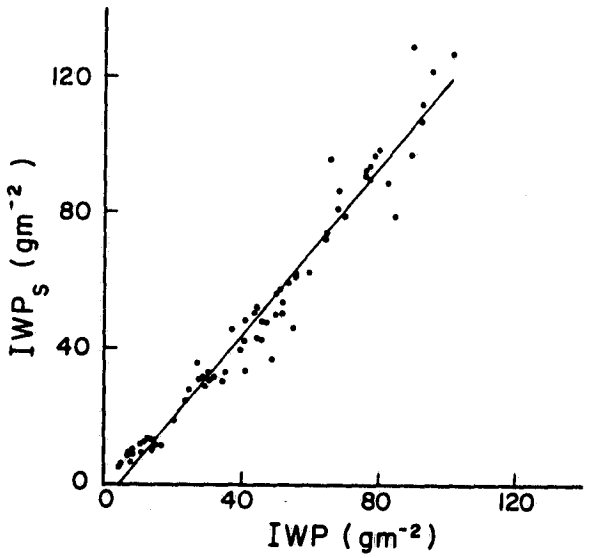

Fig. 17. Scatter plot of IWP during the October 4 case from the method of Matrosov et al. (1992) using radar and infrared radiometer data and IWP_s from the method of Sassen (1987) using radar reflectivity only. The regression line is IWP_s = 1.2 IWP - 5.4.

effects are not too strong. (Multiple scatter can cause δ_1 to increase steadily to as large as 0.4 as the pulse penetrates into an optically dense cloud.) A special case occurs when a vertically pointing lidar reflects off horizontally oriented plate crystals, which causes low δ_1.

One objective of CLARET was to establish the characteristics of depolarization in backscatter of a CO_2 lidar from ice clouds and what information the depolarization signatures could provide about clouds. The previous work regarding depolarization of backscatter from ice at CO_2 lidar wavelengths was sparse and contradictory. CLARET gathered a large body of lidar depolarization data at 10.59-μm wavelength with accompanying evidence of cloud phase from other measurements.

The CO_2 lidar uses polarization to isolate the detector from the transmitted pulse. The CO_2 normally transmits left-hand-circular polarization and detects right-hand-circular depolarization. The handedness reverses during backscatter from a spherical particle because the electric vector of the scattered light must remain aligned with the vector in the incident light. We configured the CO_2 lidar with a rotating waveplate for a slightly different depolarization ratio

$$\delta_{lc} = I_{per}/I_{cir}$$

from that of the ruby lidar, where I is the calibrated backscatter intensity normalized by the transmitted pulse energy. I_{cir} is the normal circularly polarized signal, and I_{per} is the same as the numerator of δ_1, where one linear polarization is transmitted and the orthogonal linear polarization is detected. The CO_2 switched between these two polarization modes every 1.25 s, rather than measuring both states simultaneously like the ruby lidar does.

Both lidars obtained depolarization measurements for 10 cases totaling 440 min of data. During almost all of this time, at least some cloud layers were proved to be composed entirely of ice by ruby depolarization measurements or by the fact that the cloud was colder than -40°C, which is the temperature below which homogeneous freezing occurs. The δ_{lc} for this entire set of data remained at or below a very small value of 0.02, which was the depolarization sensitivity limit of the CO_2 lidar. Details of the measurements were discussed by Eberhard (1992). An example of the results is shown in Fig. 18, where "main" and "orthogonal" refer to the denominator and numerator of the depolarization ratio, respectively.

CLARET has shown that the CO_2 lidar's depolarization is small, although only an upper limit was obtained. A CO_2 lidar cannot be used in the same way as shortwave lidars to discriminate between ice and water clouds. As suggested by Sassen (1981), the absorption at 10.59 μm by ice is so great that reflection from the first surface apparently dominates the backscatter. No mechanism exists in this reflection mode for introducing depolarization.

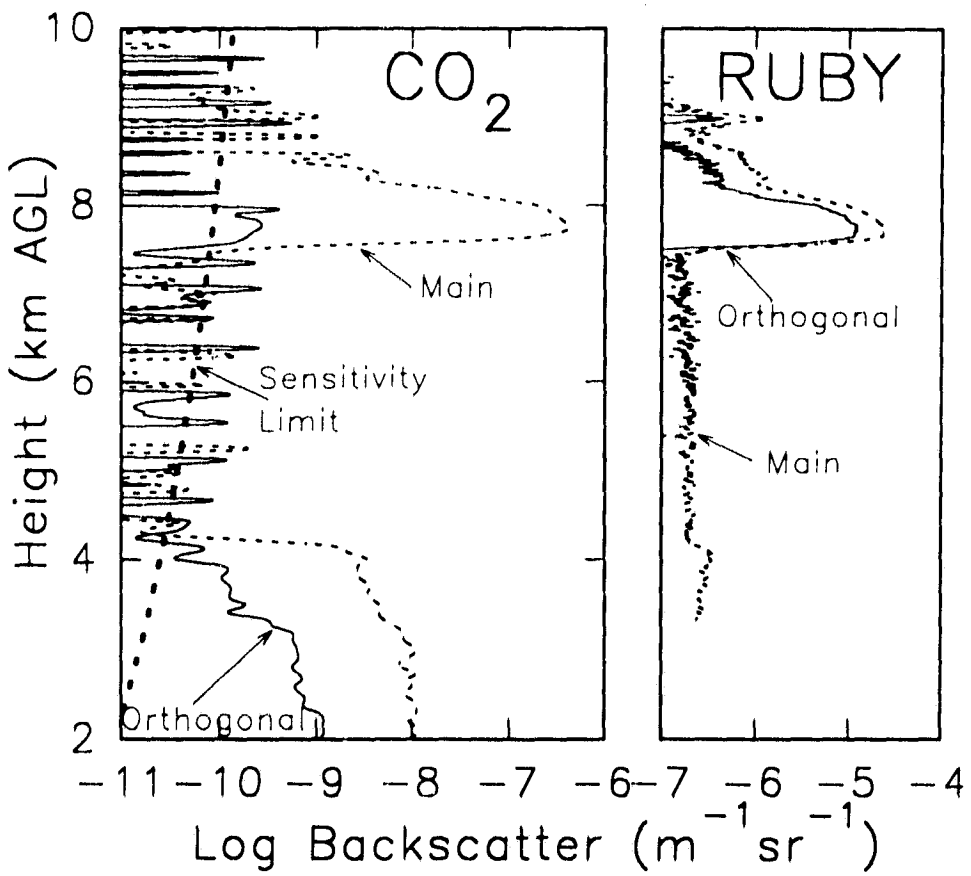

Fig. 18. Vertical profiles of main and orthogonal backscatter coefficients from an ice cloud at wavelengths of 10.59 μm (left) and 0.6943 μm (right), showing substantial depolarization in the shortwave signal (ruby lidar) but negligible depolarization for the CO_2 lidar. Data are a 20-s average beginning 0013:40 UTC on September 25, 1989.

This experimental result also suggests a simplified method for calculating the backscatter coefficient of ice particles that are much larger than the CO_2 lidar's wavelength. In this case the geometrical optics approximation applies, but only the scatter from the first surface need be calculated. This simplification could make quantitative evaluation of backscatter from complex ice crystal shapes much easier than for shortwave lidars. Therefore, the potential is excellent for quantitative study by CO_2 lidar of cirrus and other ice-containing clouds.

4.5 CO_2 Lidar Specular Backscatter Information on Ice Particles

When platelike ice crystals fall freely in the air, they tend to become oriented with their flat sides horizontal. When a zenith-pointing lidar views these, the backscatter becomes strongly enhanced compared with backscatter from the lidar with a pointing angle several

degrees off zenith. The plates act as tiny dielectric mirrors that reflect part of the laser pulse back toward the lidar when the flat sides are perpendicular to the lidar beam (Platt et al., 1978). Observations of oriented crystals can be useful in studying clouds and radiation, not only because of the information on microphysics, but also because the radiative transfer through clouds with oriented particles may be substantially different from clouds with randomly oriented particles.

An example of specular backscatter obtained by the CO_2 lidar while scanning back and forth through the zenith is shown in Fig. 19. The shape of the specular peak depends on several factors, including imperfect flatness and tilting caused by flutter, turbulence, or nonsymmetric shapes. Diffraction also spreads the width of the peak in an amount proportional to the wavelength, which for the CO_2 lidar is an order of magnitude or more larger than for shortwave lidars. If the other mechanisms for spreading the width of the specular peak are small, the approximate diameter of the plates causing the specular backscatter can be calculated assuming Fraunhofer diffraction through an aperture with the same area as the plate face. On the basis of these assumptions, the plates at 6975 m AGL in Fig. 19 were calculated to be approximately 115 μm in diameter.

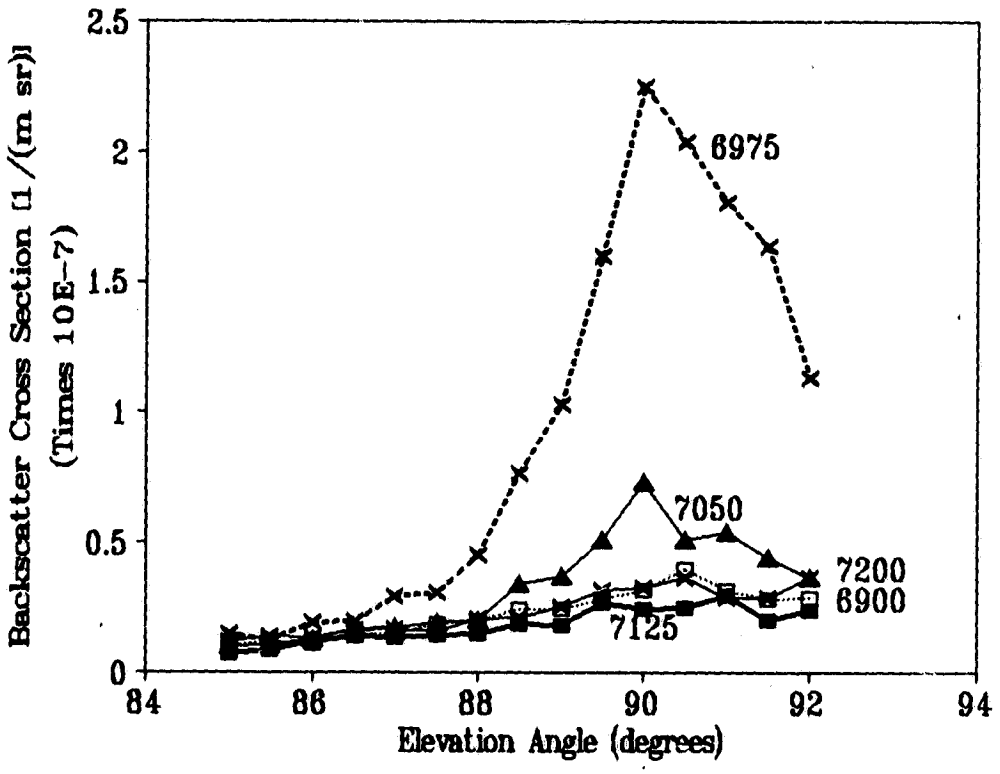

Fig. 19. Examples of specular backscatter observed by the CO_2 lidar in 75-m layers at the heights (m AGL) indicated while scanning back and forth about zenith.

During CLARET, we attempted during one case to compare the shapes of specular peaks of the ruby and CO_2 lidars scanning within about 0.5° of zenith. If diffraction dominates the spread at the longer wavelength, a noticeably narrower peak is anticipated in the ruby data. Unfortunately, the horizontal inhomogeneity of the clouds and the slow pulse rate of the ruby lidar compromised the quality of its results. The comparisons produced no examples of clear differences between the two wavelengths, but the tests were inconclusive because of the poor quality and limited number of tests.

Our research on this topic will continue with later experiments. We are investigating the possibility of enhanced backscatter for the CO_2 lidar from oriented columns and needles as well as plates.

4.6 Characteristic Drop Radius of Water Clouds

The drop size distribution in water clouds is also an important parameter for understanding the evolution of the clouds and their effects on radiative transfer. Another promising technique for CO_2 lidar is measurement of the mean or effective radius of the drop size distribution of water clouds. Development and confirmation of this technique is an important research effort in WPL, but not directly part of CLARET. Platt and Takashima (1987) proposed the concept of measuring the mode radius in their analytical study. They used Mie scattering calculations for a number of cloud size distributions to show an approximate relationship between the mode radius and the lidar's extinction-to-backscatter ratio S (in our notation). The average value of S for the penetration depth of a lidar pulse into an optically thick cloud is given by

$$S = (2B_t)^{-1}$$

where B_t is the integrated value of apparent backscatter coefficient (uncorrected for attenuation by the cloud). For optically thin clouds, S can be determined if a cooperative target is available on the opposite side of the cloud to determine the attenuation. The surface can sometimes serve this function for an airborne or spaceborne lidar. The method depends on a fortuitous relationship between extinction and backscatter at CO_2 lidar wavelengths for water drops of sizes commonly found in clouds.

We investigated the idea further by performing similar calculations for the many size distributions assembled by Pinnick et al. (1983) from the literature and research reports. We chose 10.59 μm wavelength rather than the 4.5-μm wavelength used by Platt and Takashima (1987). We found that this method is not very dependable for determining mode radius (Fig. 20) because S is an integral quantity, but mode radius depends strongly on the shape of the size distribution. Similar calculations for effective radius (Fig. 21) and mean radius (not shown) revealed a rather tight relationship between S and the radius parameter.

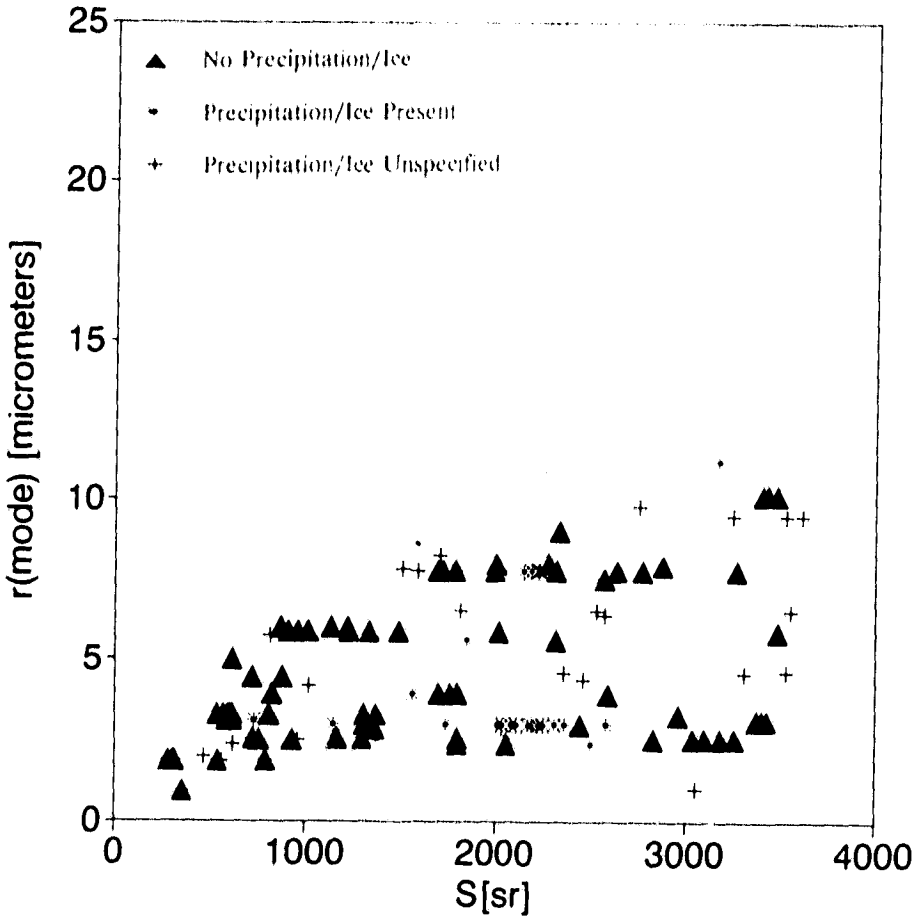

Fig. 20. Theoretical relationship between mode radius and extinction-to-backscatter ratio S at a CO_2 lidar's wavelength of 10.59 μm for the 156 measured size distributions in liquid clouds tabulated by Pinnick et al. (1983).

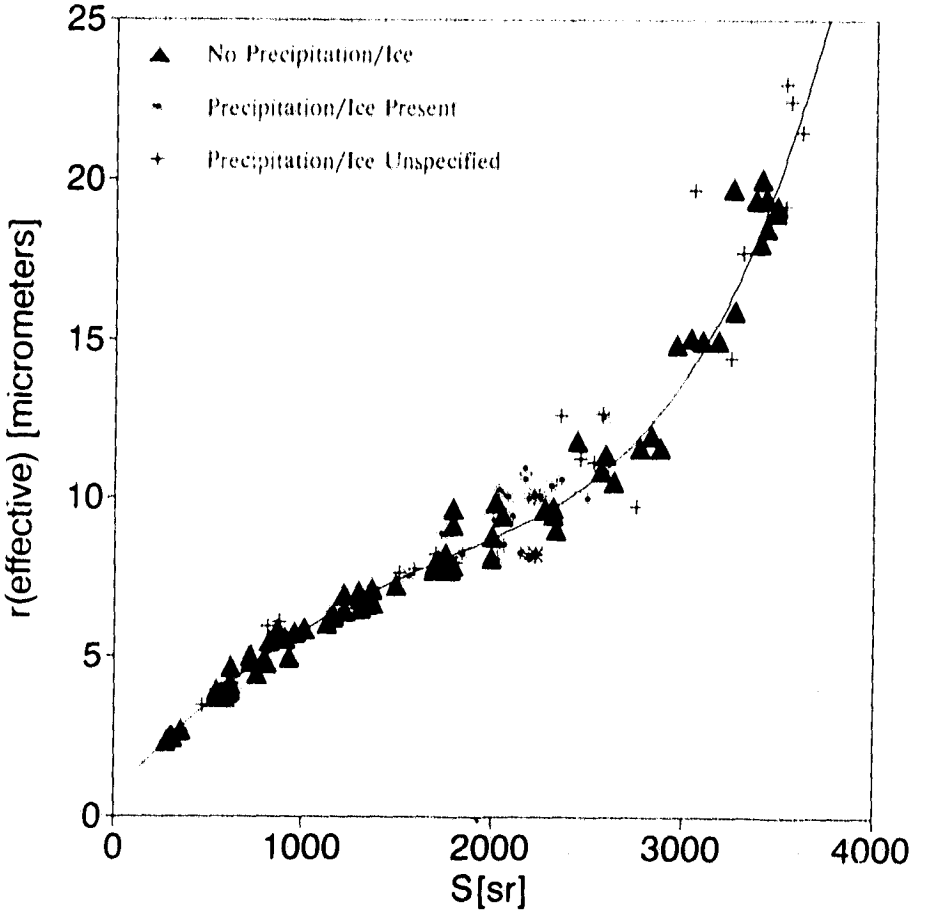

Fig. 21. Theoretical relationship between effective radius and S for the same conditions as in Fig. 20.

Some trial measurements were performed on fair-weather cumuli in Florida. The lidar stared at a constant elevation angle of about 20° while clouds advected past the beam. The height coordinate in Fig. 22 was determined by where the beam intercepted the side (or bottom) of the cloud. The values of effective radius are reasonable, and they increase with height as expected in clouds with convection still active.

After this technique is confirmed by field comparisons with other methods, it is expected to become a useful tool for studying clouds and their radiative effects.

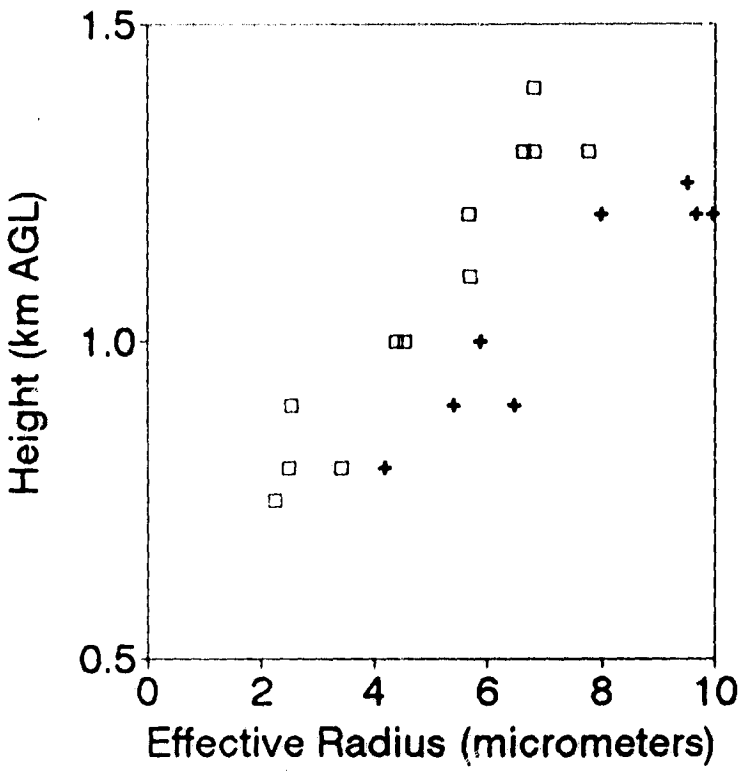

Fig. 22. Effective radius of cloud drop sizes, using the fitted curve in Fig. 21, as a function of height for fair-weather cumuli in Florida as observed from the side by a CO_2 lidar. The squares and crosses designate clouds in two different locations.

5. RECOMMENDATIONS

Our experience in CLARET leads us to several recommendations which should be valuable in guiding other cloud radiation studies such as ARM.

A combination of instruments is necessary for observing the structure of the great variety of cloud types. The information from only one or two sensors suffers serious deficiencies in many cloud conditions. We recommend a combination of lidar, cloud-sensitive radar, IR radiometer, and microwave radiometer viewing upward from the surface. At the same time, spatially resolved radiances in the infrared and visible should be measured by satellite. Temperature profiles are also needed to interpret the radiance measurements. Data from all these instruments should be processed in a coordinated manner.

These instruments complement each other. Satellites are excellent for observing cloud cover over broad areas and can provide the top heights of the uppermost layer when optically thick. However, satellite radiance measurements of thin cirrus are difficult, an overcast layer blocks the view of any lower clouds, and the cloud base heights cannot be derived directly from the radiances. Interpretation of satellite data in pixels larger than the clouds they contain is problematic at best. The range-gated backscatter measured by a surface-based lidar complements satellite measurements by observing cloud base height, the vertical structure of cirrus, and the small-scale structure of clouds. However, lidar cannot penetrate optically thick clouds. A cloud-sensitive radar penetrates well and can observe layers blocked from the view of lidar, satellite, or both. It is important to note that 8-mm or 3-mm wavelength radars have much better sensitivity for detecting clouds than the 3.2-cm wavelength radar used in CLARET. Radars have their own limitations; even the most sensitive often fail to detect some cirrus, and the reflectivity measurement is strongly biased toward precipitation rather than the radiatively important cloud droplets. The microwave radiometer and/or the depolarization data from a shortwave lidar give information on the phase (ice or water) of the clouds overhead. The infrared radiometer gives information on cloud base height or (for thin clouds) optical depth. Satellites provide information over a broad horizontal extent, whereas the surface-based sensors provide more local information with good vertical and horizontal resolution. When considered simultaneously, measurements from these various sources provide a quite complete description of basic cloud structure.

By simultaneously probing clouds, sensors like these can measure additional parameters that are important. The research described in this report on deriving information about the sizes of cirrus particles from radar-lidar or from radar-IR radiometer measurements is one important example. Another example is the LIRAD method of Platt (1979), which uses simultaneous shortwave lidar and infrared radiometer measurements to study the visible and infrared properties of cirrus. We recommend that ARM plan the capacity to derive parameters from multi-sensor observations and not restrict CART sites to parameters that can be obtained by individual instruments. The data-handling procedures should be capable of incorporating coupled processing of multi-sensor data, including algorithms that very likely

will emerge from future research. We believe that the additional multi-sensor information on clouds will prove extremely valuable for cloud-climate research.

WPL's research on cloud sensing with coherent CO_2 lidar has demonstrated excellent potential for long-term measurements of several cloud parameters. Radiation at CO_2 lidar wavelengths is much safer than that for most shortwave lidars, so CO_2 laser pulse energies can be kept high enough in an unattended system to achieve good sensitivity to even the thinnest of clouds. The development of pulsed, radio-frequency-excited CO_2 lasers at our laboratory promises to make an automated CO_2 lidar feasible. Multiple scatter in the cloud signals of most shortwave lidars seriously complicates interpretation of the backscatter, but multiple scatter is negligible for coherent CO_2 lidar. Some techniques are available at this lidar's wavelength to observe cloud parameters beyond those accessible by shortwave lidar. In addition to the methods discussed in Sections 4.5 and 4.6, we are evaluating the ability of a CO_2 lidar to observe the profile of emissivity in cirrus. We are also confident that a dual-wavelength technique now under evaluation will be at least as effective in discriminating ice, water, and mixed phase of clouds in lieu of the shortwave lidar's depolarization technique. We believe that CO_2 lidar systems can be developed that will be ideally suited for the kind of observations planned for CART.

Radars have been underutilized in past research on the radiative effects of clouds. Studies like those reported in Sections 4.2 and 4.3 are demonstrating the value of cloud-sensitive radar to a field program like CART. We believe that continuing research on radar techniques will produce even more ways by which radar can contribute to cloud observations.

Many cloud types, and some cirrus in particular, have a great degree of small-scale structure, which changes rapidly as the cloud advects overhead. Significant changes in radiative and microphysical characteristics can occur on time scales of 30 s or less. Sampling rates must be fast for studies that depend on a knowledge of detailed structure. For other purposes, the information might be horizontally (or temporally) averaged, but many aspects of the signals from remote sensors are nonlinear. ARM should be concerned about developing appropriate averaging methods for data of these kind.

Deciding on the aiming direction for the ground-based remote sensors at a CART site may seem to be trivial, but our experience at CLARET suggests otherwise. For many purposes, the measurements by ground-based remote sensors should coincide in space and time. Aiming at the zenith is the most simple, but tilting a few degrees off vertical is wise to avoid specular reflection of the lidar from oriented crystals. Another aiming mode is scanning back and forth through zenith, preferably in the cross wind direction, to observe a much larger volume of cloud. This would also enable the lidar to derive information about oriented ice crystals and would permit better matching with satellite data. However, this mode is more difficult, especially if several instruments must be scanned in unison. The scanning also adds one spatial dimension, which makes data handling more complex. We recommend that preparations for CART include careful consideration of the optimum pointing mode for the instruments.

ACKNOWLEDGMENTS

We are grateful for the assistance of Jim Allard, Brent Gordon, Kathleen Healy, Eric Holloway, Mike Jardon, Terry McNice, M.J. Post, Ron Richter, and Ann Weickmann for lidar data acquisition and processing. Bruce Bartram, Lee Church, Fernando Gonzalez, Robert Kropfli, Brooks Martner, Eric Moore, and Tim Schneider accomplished similar tasks with the radar. Radiometer and meteorological data were made available through the efforts of Richard Beeler, Mark Jacobsen, Don Nelson, Boba Stankov, and Norbert Szczepczynski. Forecast guidance from the daily weather briefers at Forecast Systems Laboratory and Pat Reddy were important to the success of CLARET I. Surface mesonet data for the October 3 case were provided courtesy of NOAA's Forecast Systems Laboratory. R.G. Pinnick supplied the water cloud size distribution data used for Figs. 20 and 21.

CLARET I and the ensuing analysis were funded jointly by NOAA, NASA, and DOE. NASA Project #4020-CL-378 from the Office of Space Science and Applications, Earth Science and Applications Division, assisted with data acquisition costs and part of the technique research. Grant #DE-AI06-91RL12089 from the Department of Energy's ARM program funded preparation of this report, processing of the accompanying data set, plus some additional technique research. We appreciate the interest of DOE in CLARET and hope these data prove valuable in this beginning phase of ARM.

REFERENCES

Cess, R.D., G.L. Potter, J.P. Blanchet, G.J. Boer, A.D. DelGenio, M. Deque, V. Dymnikov, V. Galin, W.L. Gates, S.J. Ghan, J.T. Kiehl, A.A. Lacis, H. LeTreut, Z.-X. Li, X.-Z. Liang, B.J. McAvaney, V.P. Meleshko, J.F.B. Mitchell, J.-J. Morcrette, D.A. Randall, L. Rikus, E. Roeckner, J.F. Royer, U. Schlese, D.A. Sheinin, A. Slingo, A.P. Sokolov, K.E. Taylor, W.M. Washington, R.T. Wetherald, I. Yagai, and M.-H. Zhang, 1990. Intercomparison and interpretation of climate feedback processes in 19 atmospheric general circulation models. *J. Geophys. Res.* 95:16,601-16,615.

Derr, V.E., R.S. Stone, L.S. Fedor, and H. P. Hanson, 1990. A parameterization for the shortwave transmissivity of stratiform water clouds based on empirical data and radiative transfer theory. *J. Atmos. Sci.*, 47:2774-2783.

DOE (Department of Energy), 1990. Atmospheric radiation measurement program plan. DOE/ER-0441, U.S. Department of Energy, Office of Energy Research, Washington, DC, 116 pp. (Available from the National Technical Information Service, 5285 Port Royal Rd., Springfield, VA 22161.)

Dowling, D.R., and L.F. Radke, 1990. A summary of the physical properties of cirrus clouds. *J. Appl. Meteorol.* 29:970-978.

Eberhard, W.L., 1992. Ice cloud depolarization of backscatter for CO_2 and other infrared lidars. *Appl. Opt.* 31 (in press).

Eberhard, W.L., and G.T. McNice, 1986. Versatile lidar for atmospheric studies, including plume dispersion, clouds, and stratospheric aerosol. *J. Atmos. Oceanic Technol.* 3:614-622.

Eberhard, W.L., R.E. Cupp, and K.R. Healy, 1989. Doppler lidar measurements of profiles of turbulence and momentum flux. *J. Atmos. Oceanic Technol.* 6:809-819.

Frisch, A.S., B.L. Weber, R.G. Strauch, D.A. Merritt, and K.P. Moran, 1986. The altitude coverage of the Colorado wind profilers at 50, 405, and 915 MHz. *J. Atmos. Oceanic Technol.* 3:680-692.

Hogg, D.C., F.O. Guiraud, J.B. Snider, M.T. Decker, and E.R. Westwater, 1983. A steerable dual-channel microwave radiometer for measurement of water vapor and liquid in the troposphere. *J. Clim. Appl. Meteorol.* 22:789-806.

Intrieri, J.M., W.L. Eberhard, and T. Uttal, 1991. Determination of cirrus cloud particle effective radii using lidar and radar backscatter data. Preprints, 25th International Conference on Radar Meteorology, June 24-28, 1991, Paris, France. American Meteorological Society, Boston, MA, 809-812.

Matrosov, S.Y., T. Uttal, J.B. Snider, and R.A. Kropfli, 1992. Estimation of ice cloud parameters from ground-based infrared radiometer and radar measurements. *J. Geophys. Res.* (in press).

May, P.T., K.P. Moran, and R.G. Strauch, 1988. The altitude coverage of temperature measurements using RASS with wind profiler radars. *Geophys. Res. Lett.* 15:1381-1384.

May, P.T., K.P. Moran, and R.G. Strauch, 1989. The accuracy of RASS temperature soundings. *J. Appl. Meteorol.* 28:1329-1335.

Pinnick, R.G., S.G. Jennings, P. Chylek, C. Ham, and W.T. Grandy, Jr., 1983. Backscatter and extinction in water clouds. *J. Geophys. Res.* 88:6787-6796.

Platt, C.M.R., 1979. Remote sounding of high clouds: I. Calculation of visible and infrared optical properties from lidar and radiometer measurements. *J. Appl. Meteorol.*, 18:1130-1143.

Platt, C.M.R., 1991. The experimental cloud lidar pilot study (ECLIPS) program. Topical Meeting on Optical Remote Sensing of the Atmosphere, Williamsburg, Virginia, November 18-21, 1991. Optical Society of America, Washington, DC, 163-165.

Platt, C.M.R., and T. Takashima, 1987. Retrieval of water cloud properties from carbon dioxide laser soundings. *Appl. Opt.* 26:1257-1263.

Platt, C.M.R., N.L. Abshire, and G.T. McNice, 1978. Some microphysical properties of an ice cloud from lidar observations of horizontally oriented crystals. *J. Appl. Meteorol.* 17:1220-1224.

Post, M.J., and R.E. Cupp, 1990. Optimizing a pulsed Doppler lidar. *Appl. Opt.* 29:4145-4158.

Sassen, K., 1981. Infrared (10.6-μm) scattering and extinction in laboratory water and ice clouds. *Appl. Opt.* 20:185-193.

Sassen, K., 1987. Ice cloud content from radar reflectivity. *J. Clim. Appl. Meteorol.* 26:1050-1053.

Sassen, K., 1991. The polarization lidar technique for cloud research: A review and current assessment. *Bull. Am. Meteorol. Soc.* 72:1848-1866.

Stephens, G.L., S.C. Tsay, P.W. Stackhouse, and P.J. Flatau, 1990. The relevance of the microphysical and radiative properties of cirrus clouds to climate and climatic feedback. *J. Atmos. Sci.* 47:1742-1753.

WMO (World Meteorological Organization), 1988. An Experimental Cloud Lidar Pilot Study (ECLIPS). WCRP-14, WMO/TD-NO. 251, World Meteorological Organization, Geneva, Switzerland, 36 pp.

APPENDIX A. ARTICLES ON CLARET

Eberhard, W.L., 1991. Cloud measurements by coherent lidar: Some examples and possibilities. In *Technical Digest on Coherent Laser Radar Technology and Applications, 12*. Optical Society of America, Washington, DC, 174-176.

Eberhard, W.L., 1992. Ice cloud depolarization of backscatter for CO_2 and other infrared lidars. *Appl. Opt.* (in press).

Eberhard, W.L., and M.J. Post, 1991. CO_2 lidar techniques for observing characteristic particle size of selected cloud types. Extended Abstracts, Lower Tropospheric Profiling: Needs and Technologies, September 10-13, 1991, Boulder, CO. American Meteorological Society, Boston, MA, 7-8.

Eberhard, W.L., R.E. Cupp, K.R. Healy, J.M. Intrieri, and R.J. Willis, 1991. Sensing of cloud properties with infrared lidar. Preprints, Special Session on Laser Atmospheric Studies, January 14-18, 1991, New Orleans, LA. American Meteorological Society, Boston, MA, 452-457.

Eberhard, W.L., T. Uttal, J.M. Intrieri, and R.J. Willis, 1990. Cloud parameters from IR lidar and other instruments: CLARET design and preliminary results. Preprints, 7th Conference on Atmospheric Radiation, July 23-27, 1990, San Francisco, CA. American Meteorological Society, Boston, MA, 343-348.

Intrieri, J.M., 1991. Determining cirrus cloud effective radii using lidar and radar backscatter data. M.S. Thesis, Dept. of Atmospheric Science, Colorado State University, Fort Collins, CO, 78 pp.

Intrieri, J.M., W.L. Eberhard, and G.L. Stephens, 1990. Preliminary comparison of lidar and radar backscatter as a means of assessing cirrus radiative properties. Preprints, 7th Conference on Atmospheric Radiation, July 23-27, 1990, San Francisco, CA. American Meteorological Society, Boston, MA, 354-356.

Intrieri, J.M., W.L. Eberhard, and T. Uttal, 1991. Determination of cirrus cloud particle effective radii using radar and lidar backscattering data. Preprints, 25th Conference on Radar Meteorology, June 24-28, 1991, Paris, France. American Meteorological Society, Boston, MA, 809-812.

Intrieri, J.M., G.L. Stephens, W.L. Eberhard, and T. Uttal, 1992. A method for determining cirrus cloud particle sizes using a radar/lidar backscatter technique. *J. Appl. Meteorol.* (submitted).

Intrieri, J.M., T. Uttal, R.M. Hardesty, W.L. Eberhard, and R.E. Cupp, 1991. Comparison of measurements made with NOAA's CO_2 Doppler lidar and 3.2 cm Doppler radar. Preprints, 25th Conference on Radar Meteorology, June 24-28, 1991, Paris, France. American Meteorological Society, Boston, MA, 867-870.

Matrosov, S.Y., T. Uttal, J.B. Snider, and R.A. Kropfli, 1991. Estimation of ice cloud parameters from ground-based infrared radiometer and radar measurements. *J. Geophys. Res.* (in press).

Matrosov, S.Y., T. Uttal, J.B. Snider, and R.A. Kropfli, 1992. A technique to estimate cloud particle sizes and concentrations from IR radiometer and radar measurements. Preprints, 11th International Conference on Clouds and Precipitation, August 17-21, 1992, Montreal, Canada. International Association of Meteorology and Atmospheric Physics (in press).

Uttal, T., R.A. Kropfli, W.L. Eberhard, and J.M. Intrieri, 1990. Observations on mid-latitude continental cirrus clouds using a 3.2 cm radar Comparisons with 10.6 micron lidar observations. Preprints, 7th Conference on Atmospheric Radiation, July 23-27, 1990, San Francisco, CA. American Meteorological Society, Boston, MA, 349-353.

Uttal, T., S.Y. Matrosov, J.B. Snider, R.A. Kropfli, 1992. Doppler radar measurements of ice water path and vertical velocities in optically thin clouds: CLARET I and FIRE results. Preprints, 11th International Conference on Clouds and Precipitation, August 17-21, 1992, Montreal, Canada. International Association of Meteorology and Atmospheric Physics (in press).

APPENDIX B. SURFACE MESONET STATIONS

Station Name	NWS Abbreviation	Location (County, Building)	Coordinates (Latitude, Longitude)	Altitude (feet)	Site Characteristics
Arvada	ARVC2	Jefferson, air pollution monitoring trailer, 57th and Garrison	39°48′ N 105°06′ W	5,365	Urban, slight knoll, trees, irrigation 100 ft. either side of trailer
Aurora	AURC2	Denver, WSFO at Stapleton Intl. Airport	39°46′ N 104°52′ W	5,275	Airport site, open, flat, urban area with trees to south
Boulder	BOUC2	Boulder, RL-3 at 30th and Arapahoe	40°01′ N 105°15′ W	5,290	Urban, 1-2 mi east of foothills; top of 6-story building
Briggsdale	BGDC2	Weld, 100 ft W of Hereford Rd., 1 mi N of Briggsdale	40°39′ N 104°20′ W	4,854	High, dry plains
Brighton	BRIC2	Adams, Cty. Sheriff's Dept., 19th & Bridge, Brighton, CO	39°59′ N 104°48′ W	4,985	Urban, river basin, west of sloping hill
Byers	BYEC2	Adams, private residence on Route 36	39°44′ N 104°08′ W	5,102	Flat, large garden near shelter, belt of trees 100 ft to N
Elbert	ELBC2	Elbert, Running Creek Field site	39°14′ N 104°38′ W	7,005	Rolling, grassy, no trees, glider port 1/2 mi SW
Erie	ERIC2	Weld, BAO tower site	40°03′ N 105°00′ W	5,198	Rolling farmland
Estes Park	EPKC2	Larimer, Rocky Mtn. Natl. Park Headquarters	40°22′ N 105°34′ W	7,854	Enclosed valley in mountains, moderate pine cover
Fort Collins	FORC2	Larimer, CSU Atmos. Sciences building	40°35′ N 105°09′ W	5,260	Top of 4-story building; 1/2 mi E of foothills
Fort Morgan	FTMC2	Morgan, Ft. Morgan Municipal Airport	40°20′ N 103°48′ W	4,494	Irrigated farmland 4 mi N of Platte River

(continued on next page)

APPENDIX B. (continued)

Station Name	NWS Abbreviation	Location (County, Building)	Coordinates (Latitude, Longitude)	Altitude (feet)	Site Characteristics
Greeley	GLYC2	Weld, Weld Cty. Municipal Airport	40°25′ N 104°38′ W	4,644	River bottom, irrigated farms, sprinkler under instrument shelter
Idaho Springs	ISGC2	Clear Creek	39°41′ N 105°30′ W	11,340	Peak of Squaw Mtn., 5 mi SE of Idaho Spgs.
Keensburg	KNBC2	Weld, Weld Central High School	40°04′ N 104°31′ W	4,985	Rolling irrigated farmland
Lakewood	LAKC2	Jefferson, Lakewood Fire Sta. #4 at 13155 W. Alameda	39°42′ N 105°09′ W	5,972	Suburban; first hogback of Rockies rises 1/4 m W of station
Littleton	LTNC2	Arapahoe, air pollution monitor trailer at 8100 S. University	39°34′ N 104°48′ W	5,710	Suburban, next to Highlands Reservoir (with concrete cover)
Longmont	LGMC2	Boulder, Longmont Municipal Airport	40°10′ W 105°09′ W	5,039	Flat irrigated farmland, sparse tree growth on irrigation ditches
Loveland	LVEC2	Larimer, Boyd Lake water treatment plant on U.S. Hwy. 34	40°25′ N 105°02′ W	4,965	Slightly rolling prairie, 1/4 m S of Boyd Lake
Nunn	NUNC2	Weld, Pawnee Natl. Grasslands	40°48′ N 104°45′ W	5,375	Slightly rolling prairie, very dry soil
Platteville	PTLC2	Weld, 2 mi NNW of Platteville	40°16′ N 104°52′ W	4,755	Irrigated farmland near confluence of Platte & St. Vrain rivers
Rollinsville	ROLC2	Gilpin, Fritz Peak NOAA Observatory	39°55′ N 105°29′ W	9,020	Top of mountain peak, tree cover ends below station
Ward	WRDC2	Boulder, 3 mi SW of Ward, at CU Mtn. Research Station	40°02′ N 105°32′ W	9,860	On SE side of Niwot Ridge, rocky clearing

*U.S. GOVERNMENT PRINTING OFFICE: 1992-673-025/69007